



1     **Variability in grain size, mineralogy, and mode of occurrence of Fe in surface**  
2     **sediments of preferential dust-source inland drainage basins: The case of the**  
3     **Lower Drâa Valley, S Morocco**

4     Adolfo González-Romero<sup>1,2,3</sup>, Cristina González-Florez<sup>1,3</sup>, Agnesh Panta<sup>4</sup>, Jesús Yus-Díez<sup>2,a</sup>, Cristina Reche<sup>2</sup>,  
5     Patricia Córdoba<sup>2</sup>, Andres Alastuey<sup>2</sup>, Konrad Kandler<sup>4</sup>, Martina Klose<sup>5</sup>, Clarissa Baldo<sup>6</sup>, Roger N. Clark<sup>7</sup>,  
6     Zong Bo Shi<sup>6</sup>, Xavier Querol<sup>2</sup>, Carlos Pérez García-Pando<sup>1,8</sup>

7  
8     <sup>1</sup>Barcelona Supercomputing Center (BSC), Barcelona, Spain

9     <sup>2</sup>Spanish Research Council, Institute of Environmental Assessment and water Research (IDAEA-CSIC),  
10     Barcelona, Spain

11     <sup>3</sup>Polytechnical University of Catalonia (UPC), environmental engineering doctoral programme, Barcelona,  
12     Spain

13     <sup>4</sup>Institute of Applied Geosciences, Technical University Darmstadt, Darmstadt, Germany

14     <sup>5</sup>Karlsruhe Institute of Technology (KIT), Institute of Meteorology and Climate Research (IMK-TRO),  
15     Department Troposphere Research, Karlsruhe, Germany

16     <sup>6</sup>School of Geography Earth and Environmental Sciences, the University of Birmingham, Birmingham,  
17     United Kingdom

18     <sup>7</sup>PSI Planetary Science Institute, Tucson, AZ, USA

19     <sup>8</sup>Catalan Institution for Research and Advanced Studies (ICREA), Barcelona, Spain

20     <sup>a</sup>now at: Center for Atmospheric Research, University of Nova Gorica, Ajdovščina, Slovenia.

21  
22     **Corresponding author:**

23     Adolfo González-Romero, <agonzal3@bsc.es>

24     Xavier Querol Carceller, <xavier.querol@idaea.csic.es>

25  
26  
27  
28  
29  
30  
31  
32  
33  
34  
35  
36  
37  
38  
39  
40  
41  
42  
43  
44  
45  
46  
47  
48  
49  
50  
51



52

53 **Abstract**

54 The effect of mineral dust emitted from arid and semiarid surfaces upon climate and ecosystems depends  
55 fundamentally on their particle size distribution (PSD) and size-resolved mineralogical composition.

56 ~~However, soil mineralogy atlases used for mineral-speciated dust modelling are highly uncertain as they  
57 are derived extrapolating mineralogical analyses of soil samples that are particularly scarce in dust-source~~

58 ~~regions. This extrapolation neglects processes affecting the formation of different dust-emitting  
59 surface sediments, such as dunes, crusts, and paved sediments.~~

60 The Lower Drâa Valley, an inland drainage basin and preferential dust-source located in southern Morocco, was chosen for a comprehensive analysis  
61 of sediment grain size and mineralogy. Different sediment types samples were collected, including paleo-

62 sediments, paved surfaces, crusts, and dunes, and analysed through PSD analysis of minimally and fully  
63 dispersed samples, and X-ray diffraction mineralogical analysis of bulk samples. We also performed Fe

64 sequential wet extraction to characterize Fe mineralogy, including the contents of (oxyhydr)oxides  
65 (goethite and hematite), key to dust radiative effects, and poorly crystalline pool of Fe (readily

66 exchangeable ionic Fe and nano-Fe-oxides), relevant to dust impacts upon ocean biogeochemistry. Based  
67 on the results we propose a conceptual model where both particle size and mineralogy are segregated by

68 transport and deposition of sediments during runoff of water across the basin, and by the precipitation  
69 of salts, which causes a sedimentary fractionation. Coarser particles substantially richer in quartz are more

70 present in elevated areas, and finer particles rich in clay, carbonates, and Fe-oxides are present in  
71 depressed areas, where dust emission is maximized. When water ponds and evaporates, secondary

72 carbonates and salts precipitate, and the clays are enriched in readily exchangeable ionic Fe, due to  
73 sorption of dissolved Fe by illite. Our results differ from currently available mineralogical atlases and

74 highlight the need for observationally-constrained global high-resolution mineralogical data for mineral-  
75 speciated dust modeling.

76 **Keywords:** Arid regions, dust-sources, desert dust, dust-emitting sediments formation model, dust  
77 modelling.

78

79

80

81

82

83

84

85

86

87

88

89

90

91

92

93

94

95



96 **1. Introduction**

97 Desert dust is atmospheric particulate matter (PM), mostly mineral in composition, emitted into  
98 the atmosphere by wind erosion of arid and semi-arid surfaces. The global dust source regions  
99 include North Africa, the Middle East, Central Asia, Western Australia, South America, Southern  
100 Africa and Southern US-Northern Mexico. From these regions, North Africa accounts for around  
101 50 % of the global dust emissions, followed by Central Asia, the Middle East and East Asia (Kok  
102 et al., 2021). Dust storms arise when strong winds generate a large amount of dust particles that  
103 drastically reduce visibility nearby and are transported over distances of hundreds of kilometres  
104 (Prospero et al. 2002). During transport, dust perturbs the energy and water cycles by direct  
105 radiative forcing and influences cloud formation, precipitation and the associated indirect  
106 radiative forcing (Weaver et al., 2002). Dust transports nutrients across the planet affecting  
107 ocean productivity (Boyd et al., 2007), plant nutrient gain or loss (Sullivan et al., 2007), and  
108 glacier mass budgets (Goudie & Middleton, 2006). Dust can also directly affect human health by  
109 inhalation or by favouring the propagation of diseases (Goudie & Middleton, 2006, De Longeville  
110 et al., 2010; Karanasiou et al., 2012; Pérez García-Pando et al., 2014). It can reduce renewable  
111 solar energy output due to attenuation of solar radiation and soiling of solar panels (Monteiro  
112 et al., 2022), create poor visibility on roads increasing the risk of traffic accidents (Middleton,  
113 2017) and cause disturbances in airport operations and air traffic (Monteiro et al., 2022).

114 Dust is emitted mostly from arid inland drainage basins (Dubief, 1977; Prospero et al., 2002;  
115 Goudie & Middleton, 2006; Bullard et al., 2011; Querol et al., 2019). These basins encompass  
116 different sedimentary environments, many of which are potentially efficient sources of dust,  
117 including unconsolidated aeolian deposits, endorheic depressions, and fluvial and alluvial  
118 dominated systems (Bullard et al., 2011). Consolidated or compacted fine sediments in the form  
119 of crusts and paved sediments, for instance on ephemeral lake beds, can also be important dust  
120 emitting surfaces when loose sand size sediments provided by adjacent sand dunes are available  
121 (Stout, 2003). These sand particles are efficiently mobilised by wind and ~~strike the~~ consolidated  
122 surface breaking the sediment aggregates and releasing dust (Shao et al., 2011).

123 Models developed to simulate the atmospheric dust cycle and its impact on climate represent  
124 dust emission, transport, interactions with radiation and clouds, and removal by wet and dry  
125 deposition (Tegen and Fung, 1994; Ginoux et al., 2001; Zender et al., 2004; Perez et al., 2011,  
126 Klose et al., 2021). ~~Modelling efforts have mostly focused on the representation of dust sources~~  
127 ~~and emission (Kok et al., 2021) and the characterization of dust sources is one of the crucial~~  
128 ~~aspects for representing dust mobilisation in models. Traditionally, models used aridity as a~~  
129 ~~criterion to identify potential dust sources (Tegen and Fung, 1994). Satellite retrievals~~  
130 ~~subsequently showed that the most prolific sources occupy a small fraction of arid regions~~  
131 ~~(Prospero et al., 2002; Ginoux et al., 2012).~~ These so-called “preferential sources” are found  
132 within enclosed basins, where easily eroded soil particles accumulate after fluvial erosion of the  
133 surrounding high-lands. The implementation of preferential source functions in global models  
134 based on topography (Ginoux et al., 2001), hydrology (Tegen et al. 2002; Zender et al. 2003),  
135 geomorphology (Bullard et al., 2011), or satellite proxies (Prospero et al., 2002; ~~Gioux~~  
136 ~~et al., 2012), has significantly improved the skill of models by approximately locating large-scale~~  
137 ~~natural sources. However, models are not able yet to capture the small-scale spatial and~~  
138 ~~temporal variability in emissions apparent from observation~~ ~~Some~~ studies have provided  
139 small-scale understanding on the role of geomorphology and sedimentology upon dust



140 emissions (Bullard et al., 2011; Baddock et al., 2016). For instance, Bullard et al. (2011)  
141 developed a conceptual model of how different geomorphologic surfaces affect the intensity  
142 and temporal variability in dust emissions.

143 While it is key to understand dust source location and emission intensity, climate impacts by  
144 dust also depend upon its mineralogy. Dust is a mixture of different minerals including quartz,  
145 clay minerals (mica/illite, kaolinite, palygorskite, chlorite/clinochlore and  
146 smectite/montmorillonite), feldspars (albite/anorthite and orthoclase), carbonate minerals  
147 (mainly calcite and dolomite), salts (mainly halite and gypsum), Fe-oxides and hydroxides  
148 (mostly goethite and hematite) and other oxides or hydroxides of Ti, Mn and Al (Coudé-Gausson  
149 et al., 1987; Schültz & Seibert, 1987; Molinaroli et al. 1993; Gomes, 1990; Sabre, 1997;  
150 Caquineau, 1997; Avila et al., 1997; Caquineau et al., 1998; Claquin et al., 1999; Formenti et al.,  
151 2008; Nickovic et al., 2012; Scheuven et al., 2013; Journet et al., 2014; Scanza et al., 2015; Ito  
152 & Wagai, 2017; Querol et al., 2019). The relative abundances, size, shape, and mixing state of  
153 these minerals influence the effect of dust upon climate. For instance, the absorption of solar  
154 radiation by dust depends upon the iron oxide content (Tegen et al., 1997; Sokolik and Toon,  
155 1999; Reynolds et al., 2014, Di Biagio et al., 2019), ice nucleation in mixed-phase clouds is highly  
156 sensitive to the amount of K-feldspar and quartz (Boose et al., 2016b; Harrison et al., 2019), and  
157 the bioavailability of iron in dust depends upon its iron mineralogy and speciation (Shi et al.,  
158 2012). According to the geological, geomorphological and climate (weathering) patterns of the  
159 desert regions, the type, and proportions of minerals might greatly vary (Caquineau, 1997;  
160 Caquineau et al., 1998, Claquin et al., 1999; among others). For example, Sahelian dust is  
161 composed mainly of quartz, kaolinite and hematite, while in North-eastern China and the Sahara  
162 mica/illite, kaolinite, quartz and carbonates prevail (Shen et al., 2009; Claquin et al., 1999).

163 Despite the potential importance of dust mineralogical variations, climate models typically  
164 assume dust composition as globally uniform, which is partly due to our limited knowledge of  
165 the composition of the parent sources at global scale. The few models that explicitly represent  
166 dust mineralogical composition (e.g., Scanza et al., 2015; Perlwitz et al., 2015, Li et al., 2021;  
167 Gonçalves Ageitos et al., 2023) use global atlases of soil type and the relation of this variable to  
168 soil mineralogy. This relation is inferred using massive extrapolation from a limited amount of  
169 mineralogical analyses, particularly in dust source regions, ancillary information on soil texture  
170 and colour, and a number of additional assumptions (Claquin et al., 1999; Journet et al., 2014).  
171 The mineralogical composition is characterised in two traditional grain-size ranges (Wentworth  
172 (1922) and Urquhart (1959)), i.e. clay (<2 µm) and silt (2-63 µm) linked to FAO (Food and  
173 Agricultural Organization of the United States) soil texture datasets based on measurements  
174 following wet sieving, a technique that disperses (breaks up) the mineral aggregates found in  
175 the undisturbed parent soil into smaller particles (Chatenet et al., 1996). Furthermore, the  
176 samples that underpin these atlases consider the first 10-15 cm of soil sediment, which is much  
177 deeper than the thin layer that is relevant to wind erosion and dust emission, and mineralogy is  
178 normally analysed after removing organic matter with hydrogen peroxide (H<sub>2</sub>O<sub>2</sub>), which can  
179 partially dissolve carbonate minerals.

180 The assumed relationship between mineralogy and soil type in these atlases neglects the role of  
181 geomorphology and sedimentology affecting the formation of different dust-emitting surface  
182 sediments, such as dunes, crusts, and paved sediments. In this study, we provide a  
183 comprehensive analysis of the variability in grain size, mineralogical composition and Fe



184 mineralogy and speciation of sediments collected across the Lower Drâa Valley, an inland  
185 drainage basin and prolific dust-source located in the north-western border of the Saharan  
186 desert in southern Morocco (Figure 1). The data collection was performed during a wind erosion  
187 and dust field campaign in September 2019 in the context of the FRontiers in dust minerAlOGical  
188 coMposition and its Effects upoN climaTe (FRAGMENT) project. Based on the analysis of the  
189 results we propose a conceptual model that links formation processes of potential dust-emitting  
190 sediments to their particle size distribution (PSD) and mineralogy across the basin.

191

## 192 **2. Methodology**

### 193 **2.1 The FRAGMENT field campaign and the study area**

194 The sediment samples analysed in this study were collected during a field campaign that took  
195 place in September 2019 in the Lower Drâa Valley, west of M'Hamid, between the Erg Chigaga  
196 and L'Bour (Figure 1a), a dry inland drainage basin where dust emission is frequent as evidenced  
197 by satellite data (Ginoux et al. 2012) (Figure 1b). The region lies where the Sahara Desert begins,  
198 to the south of the Atlas Mountain, near the Algerian border, in the Drâa River Basin. Preliminary  
199 results from the Earth Surface Mineral Dust Source Investigation, EMIT, (Green et al., 2020) show  
200 the presence of a complex regional mineralogy with fine-grained goethite, hematite (with  
201 substantial nano-sized hematite), gypsum sulphate salts in the lowlands (depressions) and  
202 Illite/muscovite, with local outcrops of carbonates in the study area (Figure 1c). The EMIT  
203 mineral maps show that the study area is representative of the larger area.

204 The campaign was conducted in the framework of the FRAGMENT project, in which distinct  
205 desert dust source regions are being characterised to better understand the size-resolved dust  
206 emission and composition for different meteorological and soil conditions. The aim of  
207 FRAGMENT is to better understand dust emission, its mineralogical composition and the effects  
208 of dust upon climate, by combining field measurements, laboratory analyses, remote and in situ  
209 spectroscopy, theory and modelling. FRAGMENT field campaigns consist of intensive sediment  
210 sampling and meteorological and airborne dust measurements in one specific location, along  
211 with sediment sampling across the broader basin. The intensive meteorological and airborne  
212 dust measurements were performed in the dry lake L'Bour and are analysed in e. g., González-  
213 Florez et al., 2022; Panta et al., 2022; Yus et al., in prep. Here we focus on the sediment sampling  
214 across the basin.

215 The study area records very low annual precipitation (ranging from <50 to 800 mm) and  
216 extremely variable droughts interrupted by extreme floodings (Berger et al., 2021). The Drâa  
217 River was anthropogenically dried in this area mostly due to the construction of El Mansour  
218 Eddahbi dam in 1972 (near Ouarzazate). The Jbel Hassan Brahim range reaches the highest  
219 altitude in the area (840 m.a.s.l.), while the Drâa River is the lowest point (570 m.a.s.l.). The  
220 study region corresponds to a low relief alluvial system, unarmored and unincised according to  
221 Bullard et al. (2011). Rains are scarce, but sometimes they concentrate in the mountains (high-  
222 lands) and even more sporadically they can directly affect the area during convective storms,  
223 creating flash floods with a high sediment load canalised by torrents or wadis, such as wadi  
224 Latache (high-lands) (Figure 1a), which flood flat areas. In specific areas across the basin, highly  
225 sediment-loaded waters can be shortly ponded on the way to Drâa River in small depressions,  
226 such as dry Lake Iriki, Erg Smar or L'Bour (low-lands) (Figure 1a), among other areas, along the  
227 floodplain. Dunes are concentrated in small flat areas, near depressions, where, after wind  
228 erosion, sediment can be dragged and be entrapped by the very scarce and low vegetation.



## 229 **2.2 Sediment sampling**

230 The sampled sediments include paleo-sediments (hereafter named sediments), paved  
231 sediments, crusts, and dunes, according to the classification by Watt & Valentin (1992) and  
232 Valentin & Bresson (1992). Paved sediments result from cyclic drying and aeolian erosion of the  
233 surface of paleo-sediments and range from 0.5 to 2 cm of vertical depth. Crusts ranged from 0.1  
234 to 2 cm of vertical depth and we differentiated two types: i) thin depositional crusts formed as  
235 result of the deposition of sediments from running water during floods, and ii) thicker  
236 sedimentation crusts resulting from the sedimentation and drying of highly sediment-loaded  
237 waters in ponded areas of different sizes. Sediments are below the crusts (not exposed to the  
238 atmosphere) and dunes are aeolian deposits. We used a 50 cm<sup>2</sup> inox steel shovel to sample  
239 surfaces (first top cm), sediments (below surface, from 1 to 5 cm in the vertical depth) and dunes  
240 (from surface to 5 cm). We registered coordinates, type of sample, surroundings description and  
241 we also recorded any other important information and made concept drawings. We obtained  
242 42 sediment samples, including crusts (12), dunes (12), paved sediments (11) and sediments (7)  
243 (Figure 2) from different locations in the Drâa River Basin.

## 244 **2.3 Sample treatment**

245 To analyse mineral-size fractionation (<10 and 10-63 µm) we applied a fully dispersed size  
246 fractionation using MilliQ-grade water and shaking the samples previous to separation for 12-  
247 24 h. First, samples were subjected to 250, 63 and 10 µm sieves to obtain the <63 and <10 µm  
248 fractions. Due to availability, the smallest opening size of the sieve was 10 µm. Sonic sieving was  
249 applied for 60 s at maximum sustainable power for 3 min in every sieve. Finally, subsequent  
250 drying at 80 °C was applied to recover the solid fraction from the suspension.

## 251 **2.4 Analysis**

### 252 **2.4.1 Particle size distribution and texture**

253 The particle size analysis was carried out for fully (natural aggregates totally dispersed) and  
254 minimally (natural aggregates minimally dispersed) dispersed to obtain the fully dispersed  
255 particle size distribution (FDPSD) and the minimally dispersed particle size distribution (MDPSD)  
256 to evaluate (i) how aggregates and particles occur in natural conditions (MDPSD) and (ii) the  
257 distribution of single particles that form the aggregates (FDPSD). The MDPSDs were obtained  
258 with laser diffraction using a Malvern Mastersizer 2000 Scirocco accessory (hereinafter,  
259 Scirocco) for minimally dispersed conditions. In this case, samples of 0.3-0.5 g of the fraction <2  
260 mm were introduced into the Scirocco vibration plate with a 2 mm aperture and 5 s measuring  
261 time. FDPSDs were determined using the Malvern Mastersizer 2000 Hydro G accessory  
262 (hereinafter, Hydro) with a water suspension and ultrasound assistance for totally dispersed  
263 conditions. In that case, the samples were pre-treated following the method by Sperazza et al.  
264 (2004). The suspension was introduced into the Hydro's sample container, pumping at 1750 rpm  
265 and stirring at 500 rpm. Results were obtained in both cases using the Fraunhofer method (Etzler  
266 et al., 1997).

267 To investigate the possible occurrence of vertical segregation of the PSD (top layers are the ones  
268 that are emitting dust), 7 crust and 5 paved sediment samples were selected for vertically-  
269 resolved PSD analyses. To this end, 3 sub-samples were extracted from each sample (top,



270 middle, and bottom sections) by scratching the surface with a cutter from top to bottom and  
271 were analysed separately. The thickness of these crusts varied between 4 to 8 mm.

272 The pipette method was also used to analyse the texture of a soil layer or boundary according  
273 to FAO-UNESCO (1990) of a total of six samples. This allows us to separate a suspension of the  
274 sample in MilliQ-grade water into different size fractions (>63, 2-63 and <2 µm), dry and analyse  
275 each size-fraction individually.

#### 276 2.4.2 Mineralogical composition

277 Quantitative mineralogical analyses of bulk sediment samples and segregated size fractions  
278 were carried out by means of powder X-Ray Diffraction (XRD), using a Bruker D8 A25 Advance,  
279 with Cu K<sub>α1</sub> radiation of 1.5405 Å wavelength, a Bragg Brentano geometry and a LynxEyeXE  
280 detector. Analysis was performed at 40 mA and 40 kV with a range of angles from 4 to 60° and  
281 angle steps of 0.019° and 10 Hz for 1 h/sample. The mineral identification was made with the  
282 EVA software package by Bruker. For quantitative analyses we used the method of the internal  
283 reference material by Chung (1974), with quartz as the internal reference. The ratios of  
284 intensities of the different minerals versus quartz were obtained by preparing and analysing  
285 binary mixtures of the specific minerals and quartz. The accuracy of the XRD quantitative  
286 approach was tested by analysing 16 mixtures of reference materials with known concentrations  
287 of minerals. Figure S1 summarises major results, which yield relative standard deviations versus  
288 the known contents of quartz (13 % of error), albite/anorthite (10 %), calcite (31 %), dolomite  
289 (14 %), mica/illite (29 %), kaolinite (11 %), gypsum (27 %), anhydrite (19 %), goethite (42 %),  
290 hematite (50 %).

291 For an in-depth evaluation of clay mineralogy, XRD analyses of oriented aggregates following  
292 the procedure by Thorez (1976) were carried out for the same six samples of the texture. We  
293 treat the samples for air drying (AO), glycolation (AG) and heating (AC). Mica/illite,  
294 chlorite/kaolinite, palygorskite and smectite were found in all the samples, as evidenced from  
295 the bulk XRD analysis. Calcite and dolomite were dissolved by acidifying soil suspension with a  
296 strong acid as HCl and the excess used to quantify stoichiometrically the content of carbonates  
297 using the method proposed by Horváth et al. (2005) also for the same six samples of the clay-  
298 oriented aggregates and texture.

299 To investigate the possible occurrence of mineralogical vertical segregation, the 7 crust and 5  
300 paved sediment unaltered samples used for particle size analysis (see section 2.4.1) were also  
301 used for vertically-resolved mineralogy analyses.

#### 302 2.4.3 Mode of occurrence of Fe

303 Fe is a key ingredient to climatic and biological processes affected by dust. For instance, the  
304 amount, mixing state and size of Fe-oxy/hydroxides determine the degree of absorption of solar  
305 radiation by dust (Engelbrecht et al., 2016) and the potential solubility of the dust deposited into  
306 the ocean (Shi et al., 2012). However, the XRD semiquantitative analysis for Fe-oxy/hydroxides  
307 are affected by large uncertainties due to the low concentrations (increasing relative errors) and  
308 is not sensitive to nano-Fe-oxides (Shi et al., 2012). We complemented the XRD analyses by  
309 quantifying the levels and mode of occurrence of Fe in the bulk samples using the methodology  
310 described in Shi et al. (2009), through which based on a sequential extraction we determine the  
311 amount of readily exchangeable (adsorbed) Fe ions and nano-Fe-oxides (FeA) and the amount





312 of crystalline Fe-oxides, mainly hematite and goethite (FeD) in the samples. We used 30 mg of  
313 Arizona Test Dust (ATD; ISO 12103-1, A1 Ultrafine Test Dust; Powder Technology Inc.) to test the  
314 accuracy of the method and extractions were done with 15 ml of extractant solution. For total  
315 Fe content (FeT) we used a two-step wet acid digestion method developed by Querol et al.  
316 (1993, 1997) and a coal fly ash (1633b) standard sample was used to test accuracy. The 1633b  
317 gave 7.5 % with a standard deviation of 0.14 % for total Fe (reference content of 7.8 % of Fe),  
318 while ATD gave 0.076 % with a standard deviation of 0.002 % of FeA and 0.49 % with a standard  
319 deviation of 0.07 % for FeD + FeA (reference content of 0.067 % of FeA and 0.41 % of FeD).  
320 Furthermore, by subtraction, we obtained the contents of structural Fe ( $FeS = FeT - (FeA + FeD)$ ),  
321 corresponding to the Fe fraction as elemental Fe into the structure of minerals other than Fe-  
322 oxides, such as illite or other Fe-bearing minerals. Furthermore, the FeD contents were  
323 converted stoichiometrically to hematite ( $Fe_2O_3$ ) and goethite ( $FeO(OH)$ ) by using the  
324 hematite/goethite proportions from XRD.

#### 325 2.4.5 Electron microscopy of crust and paved sediment sections

326 The PSD, mineralogy and morphology of crust and paved sediments can vary along the vertical  
327 profile, especially in crusts where progressive sedimentation and subsequent evaporation leads  
328 to inter-layering of sediments with different properties. For that purpose, crust and paved  
329 sediment sections were impregnated with epoxy resin, cut, and polished with diamond paste  
330 for microscopy analysis. The polished samples were coated with graphite before analysis with a  
331 JEOM JSM-7001F SEM-EDX Scanning Electron Microscope (SEM).

### 332 3. Results and discussion

#### 333 3.1 Regional variability

##### 334 3.1.1 Particle size distribution

335 We analyse the PSDs of the samples collected across the basin to detect possible trends or size  
336 segregation patterns from high- to low-lands for the different types of sediment. The mean  
337 median diameter values of each group of sediments provided in this section represent the mean  
338 and standard deviation of the median diameters. Because the PSDs are generally bi-modal, other  
339 PSD metrics can be found in Table 1, including the maximum, minimum and mean of the median  
340 diameters for different types of sediments, location, PSD type (MDPSD and FDPS), and size  
341 fraction (full range,  $<63 \mu m$  and  $>63$  to  $< 2000 \mu m$ ).

342 MDPSDs, excluding dune samples, show a major mode centred around  $100 \mu m$  in diameter and  
343 a secondary one between 2 to  $20 \mu m$  (Figure 3a; Table 1). FDPSD's also show two modes at 5  
344 and  $100 \mu m$  (Figure 3b; Table 1). The MDPSDs and FDPSDs of dune samples are very similar with  
345 a main mode centred around  $150 \mu m$  and a secondary small one at  $5 \mu m$  (30 times lower) (Figure  
346 3c and d). Crust samples show the largest fine ( $0-5 \mu m$ ) fraction in MDPSD, followed by paved  
347 sediments and sediments (Figure 3e). FDPSDs show a similar trend but with a larger proportion  
348 of fine particles compared to MDPSD (Figure 3f).

349 The mean median diameter of the MDPSDs (Figure 4a), excluding dune samples, is  $88 \pm 63 \mu m$ ;  
350 and that of the FDPSDs, is  $27 \pm 51 \mu m$  (Figure 4a). Therefore, aggregates are about 3 times coarser  
351 than individual mineral particles. As expected, dunes were coarser than other types of  
352 sediments, with a mean median diameter of  $219 \pm 70 \mu m$  of the FDPSDs, which is very similar to





353 that of the MDPSDs (Figure 4b). The mean median diameters of MDPSDs are  $70\pm 48$ ,  $74\pm 45$  and  
354  $113\pm 79$   $\mu\text{m}$  for sediments, paved sediments and crusts, respectively (Figure 4c); whereas the  
355 mean diameters of FDPDSs are  $19\pm 11$ ,  $21\pm 26$  and  $37\pm 77$   $\mu\text{m}$  for sediments, paved sediments  
356 and crusts respectively, about 3 to 4 times finer (Figure 4d).

357 The spatial variation of the mean diameter of the FDPDSs (Figure 5) shows coarser crusts ( $>40$   
358  $\mu\text{m}$ ) close to the high-land areas, and finer crusts ( $<40$   $\mu\text{m}$ ) near the Drâa River, likely due to  
359 flooding (causing transport and deposition of fine sediments, especially in the low-lands) caused  
360 during scarce and intensive rains. For paved sediments, sediments and dunes, spatial PSD trends  
361 were not evident, with mean median diameters ranging from 10 to 120, 10 to 40 and 120 to 300  
362  $\mu\text{m}$ , respectively, randomly located across the basin (Table 1).

363 According to the size classification by Valentin & Bresson (1992) and using the FDPDS data  
364 (Figure S2), dune samples can be classified as sand, loamy sand, and sandy loam; sediments as  
365 silt loam and loam; paved sediments as sandy loam, loam and silt loam; and crusts as sandy  
366 loam, loam, silty clay loam and silt loam. As shown in Figure S2 and due the higher transport  
367 potential of clays during rain episodes, and their accumulation during ponding, crusts tend to be  
368 further enriched in clay fractions, especially in low-lands, compared to paved sediments and  
369 sediment samples (see section 3.4).

### 370 3.1.2 Mineralogical composition

371 We describe here the mineralogy of samples collected across the basin to detect possible trends  
372 or mineral segregation patterns from high- to low-lands for the different types of sediment. The  
373 mineralogical composition (mass % composition of the bulk sample) of dunes, crusts, paved  
374 sediments and sediment samples is summarised in Table 2. Dunes show a homogeneous  
375 mineralogy across the study area, with mineral abundances of  $74\pm 9.7$  % quartz,  $5.8\pm 2.9$  %  
376 calcite,  $6.7\pm 3.6$  % microcline,  $6.9\pm 3.1$  % albite/anorthite,  $4.1\pm 2.3$  % clay minerals,  $1.0\pm 1.4$  %  
377 dolomite,  $0.38\pm 0.26$  % goethite and  $0.12\pm 0.11$  % hematite and trace amounts of halite and  
378 gypsum ( $<0.1$  %) (Figure 6). In comparison to dunes, crusts are depleted in quartz ( $48\pm 11$  %) and  
379 feldspars ( $5.0\pm 2.1$  % albite/anorthite and  $4.4\pm 3.1$  % microcline), and enriched in clay minerals  
380 ( $17\pm 8.0$  %), calcite ( $19\pm 8.0$  %), dolomite ( $3.0\pm 1.3$  %) and Fe-oxides ( $0.24\pm 0.28$  % hematite and  
381  $0.42\pm 0.56$  % goethite) (Figure 6). The content of gypsum ( $0.23\pm 0.56$  %) and halite ( $2.9\pm 5.1$  %) is  
382 higher than in dune samples, but variability is large because it depends on the exact point of  
383 crust sampling. Paved sediments have a similar mineralogy than crusts, for quartz ( $51\pm 8.7$  %),  
384 calcite ( $17\pm 4.9$  %), clay minerals ( $16\pm 7.3$  %), albite/anorthite ( $6.3\pm 1.8$  %), microcline ( $4.5\pm 2.5$  %),  
385 dolomite ( $3.5\pm 0.79$  %), hematite ( $0.34\pm 0.25$  %), and goethite ( $0.38\pm 0.38$  %), but with lower  
386 content of gypsum ( $<0.1$  %) (Figure 6). Sediments are also similar to paved sediments and crusts  
387 with a mean quartz content ( $55\pm 11$  %), calcite ( $17\pm 4.6$  %), clay minerals ( $14\pm 6.8$  %),  
388 albite/anorthite ( $5.8\pm 1.5$  %), microcline ( $3.7\pm 1.6$  %), dolomite ( $3.4\pm 1.3$  %), hematite ( $0.28\pm 0.37$   
389 %) and goethite ( $0.37\pm 0.32$  %). Trace amounts of gypsum ( $<0.1$  %) and halite ( $0.32\pm 0.55$  %) were  
390 also found in sediments (Figure 6).

391 In comparison with the bulk sediment, the fully dispersed silt fraction ( $10$ - $63$   $\mu\text{m}$ ) shows a lower  
392 amount of quartz ( $35\pm 6.4$  %) and feldspars ( $7.4\pm 2.5$  %), a higher content of carbonates ( $25\pm 5.2$   
393 %), clays ( $22\pm 10$  %) and hematite ( $1.07\pm 0.38$  %) and a similar content of goethite ( $0.61\pm 0.32$  %).  
394 In the fully dispersed  $<10$   $\mu\text{m}$  sieved fraction, the amount of quartz ( $23\pm 5.2$  %) and feldspars  
395 ( $4.7\pm 1.1$  %) is two times lower than in the bulk sediments. The fraction of carbonates remains



396 similar ( $21 \pm 9.0$  %) and the content of clays increases substantially ( $38 \pm 9.8$  %) compared to the  
397 bulk and silt-size mineralogy. The Fe-oxide content increases by about a factor two for both  
398 hematite ( $2.2 \pm 2.0$  %) and goethite ( $1.8 \pm 1.2$  %). Table 3 compares our mineralogical results in the  
399 clay and silt size ranges, both with the fully dispersed separation and the pipette methods,  
400 against the corresponding values provided by the available global mineralogical atlases of  
401 Claquin et al. (1999) and Journet et al. (2014), which assume our sample locations to be either  
402 fluvisols or yermosols in terms of soil type. In the silt-size fraction, we find similar contents of  
403 quartz, total clay, mica/illite, chlorite+kaolinite, calcite and Fe-oxides, but 3 times less feldspars  
404 and 5 times more dolomite. Compared to the clay-size fraction in the atlases, our  $<10$   $\mu\text{m}$   
405 fraction, shows larger content of quartz and feldspars (by factor of 2 to 4), a 30 % lower total  
406 clay content and similar contents of calcite and Fe-oxides, which can only be partly explained by  
407 the difference in the size fraction considered ( $<10$   $\mu\text{m}$  vs  $<2$   $\mu\text{m}$ ) as shown by the results obtained  
408 with the pipette method. Because kaolinite and chlorite have coincident spacing at 7 Å in the  
409 XRD spectra, in current atlases these minerals may be confounded, whereas in our study we  
410 quantified chlorite separately by identifying other minor peaks in the spectra. This is relevant as  
411 both minerals are very different in terms of chemical composition. In our study, we also detected  
412 minor concentrations of dolomite and traces of smectite and palygorskite. The large differences  
413 in the silt-size feldspar content may be largely due to the lack of data and coarse assumptions  
414 used in current atlases.

415 In our analysis of trends in mineralogy from the high-lands to the low-lands we considered all  
416 sample types except dunes. The low-lands, such as L'Bour and Erg Smar, are enriched in clay  
417 minerals ( $17 \pm 9.6$  and  $14 \pm 3.4$  %, respectively) compared to the high-lands ( $9.1 \pm 0.97$  %) (Figure  
418 6). Mica/illite is the most common clay mineral reaching mean contents of  $9.1 \pm 4.8$ ,  $8.1 \pm 2.0$  in  
419 Erg Smar and L'Bour, respectively, and  $5.0 \pm 0.70$  % in the high-lands. Kaolinite reaches  $7.2 \pm 5.4$ ,  
420  $4.9 \pm 2.1$  and  $3.5 \pm 0.30$  % and clinocllore  $1.7 \pm 1.8$ ,  $1.3 \pm 0.67$  and  $0.49 \pm 0.38$  %, respectively.  
421 Smectite and palygorskite were detected only in trace amounts ( $<0.1$  %) in most samples, with  
422 only palygorskite at Erg Smar and high-lands reaching a mean content of  $0.34 \pm 0.58$  and  
423  $0.15 \pm 0.06$  %, respectively. The same trend is found for calcite ( $24 \pm 13$ ,  $16 \pm 3.1$  and  $11 \pm 2.7$  %, Erg  
424 Smar, L'Bour and high-lands), dolomite ( $5.0 \pm 5.1$ ,  $3.6 \pm 0.51$  and  $1.7 \pm 0.50$  %, at Erg Smar, L'Bour  
425 and high-lands) and Fe-oxides ( $0.78 \pm 1.4$ ,  $0.37 \pm 0.43$  and  $0.08 \pm 0.04$  % for hematite at Erg Smar,  
426 L'Bour and high-lands and  $0.42 \pm 0.51$ ,  $0.39 \pm 0.35$  and  $0.32 \pm 0.21$  % for goethite at Erg Smar, L'Bour  
427 and high-lands) being steeper for hematite than goethite (Figure 6). Quartz follows an opposite  
428 trend, increasing towards the high-lands ( $42 \pm 18$ ,  $53 \pm 5.0$  and  $61 \pm 5.4$  %, at Erg Smar, L'Bour and  
429 high-lands, respectively) (Figure 6). Albite/anorthite and microcline do not show a clear trend,  
430 with  $5.5 \pm 2.3$ ,  $5.9 \pm 1.8$  and  $5.4 \pm 1.2$  % at Erg Smar, L'Bour and high-lands, and  $3.4 \pm 2.4$ ,  $5.0 \pm 3.4$  and  
431  $4.6 \pm 1.7$  %, respectively (Figure 6). Salt concentrations peak randomly and depend on very local  
432 scale conditions, being higher at concave areas where ponding is favoured (see section 3.4). The  
433 mean content of halite is  $1.0 \pm 2.2$ ,  $<0.1$  and  $4.0 \pm 7.7$  % at Erg Smar, L'Bour and high-lands and  
434 that of gypsum is  $0.18 \pm 0.35$ ,  $<0.1$  and  $0.15 \pm 0.92$  %, respectively (Figure 6).

435 A soft crust occurred on the surface of several dunes (Figure 2). The PSD and mineralogical  
436 analysis of the crust and the underlying sands did not reveal significant differences. Pye & Tsoar  
437 (2015) reported that surface hardening of dunes is due to the scavenging and deposition of clays  
438 from suspended dust in light rains and by cementation of sand grains (meniscus) by precipitation



439 of carbonates and silica in the retained interstitial pore water. In both cases the potential  
440 variability caused by the slight increase of this clay and carbonate/silica cementation is obscured  
441 by variations in the bulk mineralogy.

### 442 **3.2 Vertical segregation in crust and paved sediments**

443 The examination of thin vertical cross-sections provides insight into how particle size and  
444 mineral composition vary within the top few  $\mu\text{m}$  or mm of the surface. These differences are  
445 relevant to the mineralogy and PSD of newly emitted dust.

446 The MDPSDs of crust sections (top, middle and bottom) are very similar, with two modes of  
447 occurrence at 5-7 and 200  $\mu\text{m}$  (Figure S3a). Yet, while the FDPDs show similar two modes at 1-  
448 5 and 100  $\mu\text{m}$  for the top and middle sections and a second mode at 300  $\mu\text{m}$  for the bottom  
449 section (Figure S3b). The MDPSD mean median diameter of the 7 crust profiles reach  $25\pm 25$ ,  
450  $54\pm 80$  and  $25\pm 26$   $\mu\text{m}$  for the top, middle and bottom sections, respectively, while FDPD means  
451 are  $9.4\pm 9.4$  and  $11\pm 9.5$   $\mu\text{m}$  in the top and middle sections and  $94\pm 145$   $\mu\text{m}$  in the bottom one  
452 (Figure S3c and d). Therefore, during the initial stages of ponding, coarser particles are deposited  
453 first while finer particles remain suspended (see section 3.4) in the later stages before  
454 evaporation of the water. Even some oxides, carbonates and salts may precipitate in the top  
455 layers of the crust as water evaporates and the ionic strength increases.

456 No vertical PSD segregation is observed in paved sediments, but some top sections analysed  
457 show enrichment in coarser fractions in FDPD (the median diameter increases from bottom  
458 and middle sections ( $14\pm 6.8$  and  $12\pm 5.8$   $\mu\text{m}$ ) to the top section ( $23\pm 28$   $\mu\text{m}$ )), likely due to  
459 preferential erosion of finer fractions through sandblasting (see section 3.4).

460 The mean levels of quartz and feldspars are enriched in the bottom sections of the crusts ( $46\pm 17$   
461 and  $8.7\pm 4.6$  %, respectively) compared to the middle ( $38\pm 11$  and  $8.3\pm 2.5$  %) and top sections  
462 ( $41\pm 12$  and  $6.9\pm 2.2$  %) due to the higher quartz content of the coarse fraction that is deposited  
463 first (see section 3.4). The content of clay minerals, salts and Fe-oxides is similar in the top  
464 ( $20\pm 7.2$ ,  $<0.1$  and  $3.3\pm 1.9$  %, respectively), middle ( $21\pm 5.0$ ,  $<0.1$  and  $2.8\pm 1.6$  %), and bottom  
465 sections ( $19\pm 9.1$ ,  $<0.1$  and  $1.9\pm 1.0$  %). Carbonate minerals are relatively homogeneous, but  
466 slightly enriched in the middle and top sections ( $29\pm 9.7$  and  $28\pm 7.9$  %, respectively) compared  
467 to the bottom section ( $24\pm 8.4$  %). This can arise from both detrital carbonate particles and  
468 precipitation from high ionic strength waters that are ponded and dried in the low-lands.

469 The mineral composition of the paved sediment profiles differs slightly from that of crust  
470 profiles. This is because the latter are affected by particle segregation during transport and  
471 subsequent sedimentation. The top section of the paved sediment profiles has more quartz than  
472 in the middle and bottom sections ( $44\pm 8.1$ ,  $38\pm 5.7$  and  $40\pm 9.8$  %, respectively), whereas  
473 feldspars decrease from the bottom and middle to the top sections ( $9.1\pm 4.2$ ,  $9.3\pm 2.2$  and  $6.9\pm 2.7$   
474 %). Carbonates and clay are relatively homogeneous ( $26\pm 4.9$ ,  $26\pm 2.0$  and  $25\pm 4.2$  % for  
475 carbonates, and  $22\pm 8.4$ ,  $23\pm 9.2$  and  $25\pm 4.9$  % for clays, respectively). The slight depletion of  
476 minerals in the top section may be due to sandblasting, which tends to erode the fine fraction  
477 of the surface over time (see section 3.4). Fe-oxides are more present in the top section than in  
478 the middle and bottom sections ( $2.1\pm 0.47$ ,  $2.0\pm 0.38$  and  $1.7\pm 0.27$  %, respectively) and the  
479 presence of salts is very low ( $<0.1$  % for all sections).



480 **3.3 Mode of occurrence of Fe**

481 We implemented a sequential Fe extraction procedure to evaluate the levels and mode of  
482 occurrence of Fe in dust samples from the basin. Due to limitations of XRD analysis for low Fe-  
483 oxide contents, this procedure provided a much more precise quantitative evaluation.

484 The mean FeT content of bulk crusts, paved sediments and sediments was found to be  $3.6 \pm 0.71$ ,  
485  $3.4 \pm 0.47$ , and  $3.2 \pm 0.44$  %, respectively, while bulk dunes had a much lower FeT content  
486 ( $2.0 \pm 0.33$  %). Fe-speciation studies reveal that FeS percentage from FeT (FeS/FeT) is the  
487 prevailing Fe mode of occurrence ( $67 \pm 2.4$ ,  $69 \pm 3.0$ ,  $68 \pm 2.7$  and  $73 \pm 5.9$  % in crusts, paved  
488 sediments, sediments and dunes, respectively), followed by FeD percentage from FeT (FeD/FeT)  
489 ( $31 \pm 2.3$ ,  $29 \pm 3.0$ ,  $30 \pm 3.0$ ,  $26 \pm 5.8$  %), and FeA percentage from FeT (FeA/FeT) ( $1.9 \pm 0.55$ ,  $1.7 \pm 0.56$ ,  
490  $1.4 \pm 0.55$  and  $1.0 \pm 0.54$  %). These results show that FeT is very similar between crusts, paved  
491 sediments and sediments while FeT in dunes is depleted by almost 50 %. Compared to Shi et al.  
492 (2011) samples from northwestern Africa, our sample is depleted in total iron (4.7 % FeT from  
493 Shi et al. (2011)), quite similar in FeS (67 % from Shi et al. (2011)), similar in FeD (33 % from Shi  
494 et al. (2011)) and much higher in FeA (0.43 % from Shi et al. (2011)).

495 The mean FeT content in the basin is similar in Erg Smar ( $3.6 \pm 0.27$  %) and L'Bour ( $3.2 \pm 0.66$  %)  
496 compared to high-lands ( $3.0 \pm 0.24$  %). The ratio FeA/FeT was slightly higher at Erg Smar ( $1.9 \pm 0.53$   
497 %) but similar at L'Bour and high-lands ( $1.3 \pm 0.44$  and  $1.5 \pm 0.47$  %, respectively). This is probably  
498 due to the preferential accumulation of exchangeable and nano-Fe-Oxides (FeA) in the low-  
499 lands, where flooding results in red-water ponds and red surfaces after drying. Subsequently,  
500 highly concentrated ionic Fe is trapped in the last stages of ponding, and nano-Fe-oxides may  
501 precipitate during drying. Once the ponded is dried, the crusts of the low-lands tend to have a  
502 reddish patina (see section 3.4). However, a slightly higher mean FeD/FeT of  $33 \pm 2.4$  % is  
503 obtained in the high-lands compared to  $31 \pm 2.7$  and  $29 \pm 2.4$  % at L'Bour and Erg Smar,  
504 respectively. The FeS/FeT mean content is slightly lower at the high-lands ( $65 \pm 2.5$  %) compared  
505 to Erg Smar and L'Bour ( $69 \pm 2.6$  and  $68 \pm 2.6$  %, respectively).

506 FeD levels were apportioned between hematite and goethite using XRD proportions. These  
507 results show that in crusts,  $0.79 \pm 0.66$  % of hematite and  $0.55 \pm 0.67$  % of goethite are present, in  
508 paved sediments  $0.83 \pm 0.51$  and  $0.64 \pm 0.54$  %, in sediments  $0.73 \pm 0.58$  and  $0.69 \pm 0.59$  %, and in  
509 dunes  $0.20 \pm 0.17$  % and  $0.68 \pm 0.24$  %.

510 The proportions of FeD + FeA are higher in crusts, probably due to preferential transport of non-  
511 FeS to the low-lands and the trapping of Fe ions (FeA) by clay adsorption during ponding, and  
512 the formation of nanosized Ferrihydrite ( $\text{Fe}_{4-5}(\text{OH},\text{O})_{12}$ ). This readily exchangeable Fe has very low  
513 impact on radiative forcing but a high impact in Fe fertilisation of oceans during dust events  
514 (Gobler et al., 2001), as ionic Fe adsorbed by clays and nano-Fe-oxides are easily released in  
515 water solutions. The correlation of FeS, FeD and FeA with FeT is linear, with coefficients of  
516 determination ( $R^2$ ) reaching 0.96, 0.89 and 0.67 for FeS, FeD and FeA respectively (Figure S4).  
517 Thus, when increasing total Fe content all modes of occurrence of Fe increase, but the increase  
518 is preferentially driven by FeS, while it seems that the basin FeA segregation causes a lower  
519 correlation with FeT.



520 **3.4 Conceptual model for grain size and mineralogy fractionation in crusts and paved**  
521 **sediments**

522 According to Bullard et al. (2011) and as previously discussed in this study, heavy rainfall results  
523 in the selective deposition of coarser particles from runoff and floodwaters in higher elevations.  
524 Conversely, smaller particles enriched in clays, colloidal Fe-oxides (which give the water a  
525 reddish hue), and dissolved salts tend to be transported to lower elevations. Figure 7  
526 summarises a conceptual model that outlines the formation of crusts and paved sediment in the  
527 study area, with a focus on particle size and mineralogical fractionation.

528 In the low-lands, floodwaters carrying fine sediments flood extensive flat areas, such as Erg Smar  
529 or Iriki lake. Prospero et al. (2002), Bullard et al (2011) and Ginoux et al (2012), among others,  
530 have shown that dust emissions originate from relatively small and localised areas where  
531 sediments are supplied by floodwaters, and that the occurrence of dust emissions from these  
532 areas may be partly due to the occurrence or absence of floodings. During ponding in low-lands,  
533 coarser particles deposit first and form a high sand-rich bottom layer of the crust (as described  
534 in section 3.2) (Figure 7a & 8a). Subsequently, the clay fraction deposits on top of the bottom  
535 layer until total dryness (Figure 7a & 8a) forming a second clay-rich fraction layer in the crust.  
536 However, the particle size in crust surfaces is heterogeneous (Figure S5 & S6), which can result  
537 in erodible dust-emitting sediment (heterogeneity enhances sandblasting). The finer and more  
538 easily exchangeable FeA fraction remains in suspension until the last drying stages on the most  
539 superficial layer of the crust, during drying out of the remaining ponds (as described in section  
540 3.3) (Figure 7a & 8a). During this ponding, dissolved Fe ions interact with clays in such a way that  
541 they can be adsorbed on clay surfaces according to the ionic composition of the waters (as  
542 described in section 3.3) (Echeverría et al., 1998). This typical ion adsorption by clays is higher  
543 for montmorillonite than for other clays but the content of montmorillonite is low compared to  
544 illite. In this study a high correlation is obtained for FeA and illite contents (Figure S7).  
545 Furthermore, crusts contain a higher proportion of hematite(oxide)/goethite(hydroxide) in the  
546 FeD, due to the weathering with water during transport and ponding and precipitation of nano-  
547 Fe-oxides during drying.

548 After the pond drying, the continuous heating of the clay rich surface layer causes the hardening  
549 of the crust and mud-cracking, giving a 'ceramic-like' compactness to the thick crusts in the low-  
550 lands, usually with a reddish colour induced by the Fe-oxides (Figure S5a). Complete drying  
551 causes mud cracks due to loss of volume, breaking the crust into polygonal pieces, whose  
552 thickness and area depend on the amount of clay deposited. Furthermore, these concave mud-  
553 crust pieces resulting from the cracking usually have a grey-colour patch in the middle due to  
554 the superficial precipitation of salts, which together with carbonates accumulate by capillarity  
555 (see section 3.1.2) (Figure S5b). This capillary ascension and precipitation of salts (the latter  
556 being an expansive process) causes sponging and breaking of the surface layers. Thus, a third  
557 (top) layer is formed in the crusts of the low-lands, which is very easily eroded by wind because  
558 of the spongy structure and enriched in clay and readily exchangeable Fe. In some cases, in Erg  
559 Smar, we observed an additional breaking and sponging of the third (upper layer) due to  
560 expansive clays. Both the ceramic-like compactness and the cementing of salts give the fine-clay  
561 rich crusts in the low-lands a compact pattern with coarser MDPSD compared with the high-  
562 lands where ponding is limited and very thin crusts occur. This could explain why the crusts from



563 the low-lands have finer FDPDs and coarser MDPSDs compared to the high-lands (see section  
564 3.1.1). Also, wind erosion of the few top millimetres of these crusts may result in dust with higher  
565 contents of clay, Fe-oxide and salts compared to a 15 cm sediment profile.

566 In the high-lands, washout erosion occurs during rainfall, leading to the formation very thin  
567 crusts in reduced areas. This results in sources of dust made of very thin crusts and fields of  
568 stony surfaces with lower emission rates compared to the low-lands (Bullard et al., 2011). As  
569 illustrated in Figure S6 the surfaces of paved sediments and their thin crusts might resemble  
570 crusts profiles, but with the top section depleted on clay minerals due to preferential erosion  
571 over time, and with a very thin layer (a few micrometres) of clay minerals from the previous  
572 intact formed crust after flooding or running water. The top paved sediments are more compact,  
573 finer and have homogeneous distribution of the particle than crusts, which makes them less  
574 erodible and less likely to emit dust compared to crusts (which have heterogeneous particle size,  
575 see section 3.2).

#### 576 **4. Conclusions**

577 This study analysed the particle size and mineralogy of dust-emitting sediments in the region of  
578 Drâa basin in Northern Africa, at the northwestern fringe of the Sahara. The study aimed to  
579 compare these patterns for different types of sediments and their variations across the basin.  
580 The results are consistent with the conceptual models of dust emission sources in desert areas  
581 of Prospero et al. (2002) and Bullard et al. (2011), which predict higher dust emissions in the  
582 low-lands than in the high-lands. The study shows a clear size and mineralogical fractionation  
583 between paleo-sediments and low-land dust-emitting sediments, indicating that collecting  
584 samples of parent paleo-sediments for particle size and mineralogy may not fully represent the  
585 highly emitting dust sources.

586 Both PSDs and mineralogy are segregated by transport and deposition of sediments during  
587 runoff of water across the basin, and by the precipitation of salts, which causes a sedimentary  
588 fractionation. Coarser particles such as quartz, feldspars, and carbonates (detrital) deposit first  
589 due to friction and gravity and are enriched in high-lands. In contrast, waters reaching the low-  
590 lands are enriched in fine particles (clays), carbonate, salt and Fe ions from partial dissolution of  
591 minerals of the source lands. When these waters are ponded in low-lands, coarser minerals  
592 deposit first, followed by a second layer enriched in clays minerals. Evaporation of the last  
593 ponded water layer causes the deposition of the finest particles and clays enriched in readily  
594 exchangeable ions of Fe. Once dried, the heating of the surfaces by insolation causes  
595 evaporation of interstitial solutions moving towards the surface by capillarity, leading to the  
596 precipitation of salts and secondary carbonates in the upper layer. This expansive process  
597 sponges the surface of the crust, in some cases accelerated by the occurrence of expansive clays,  
598 which might favour dust emission from a top clay-Fe-salts rich micro-layer. Therefore, dust  
599 emission is not only higher but also has a different mineral composition in the low-lands than in  
600 high-lands that is also controlled by the type of sediment.

601 Our results show that modeling mineral-speciated dust emission requires understanding of the  
602 the mineralogical and size fractionation of accumulated sediments across inland enclosed  
603 basins. Large areas may act as sediment suppliers, while reduced areas may act as dust emitters



604 with differences in sediment composition. Models that represent mineral-speciated dust  
605 emission and transport should be developed to properly account for these factors.

606 Our results have also shown that global atlases fail to describe the clay-size fraction of dust-  
607 emitting sediments in the region, overestimating the clay mineral content and underestimating  
608 that of quartz, feldspars, and Fe-oxides. Quartz and feldspars are overestimated and clay  
609 minerals underestimated in the silt-size fractions. Kaolinite-chlorite are not differentiated, while  
610 our study observes major differences. The classical procedure loses salts during fractionation,  
611 and Fe-oxides are detected mainly by color without precision. Our study detects dolomite,  
612 palygorskite, and smectite, and provides more precision for Fe-oxides, with the mode of  
613 occurrence of Fe in different types of samples and locations. However, the study was unable to  
614 obtain a sample below 10  $\mu\text{m}$  without losing salts in the process.

615 Dust models need global observationally constrained high-resolution mineral maps, which will  
616 soon become available based on high-quality spaceborne spectroscopy measurements  
617 performed from the International Space Station (Figure 1c, Green et al., 2020). A key challenge  
618 of mineral mapping based on spectroscopy for dust emission modeling is to constrain not only  
619 the presence (Figure 1c) but also the abundance of the different surface minerals. The data  
620 gathered and analysed in this study will be used to evaluate these spaceborne retrievals in  
621 forthcoming studies.

622

623

624

625

626

627

628

629

630

631

632

633

634

635

636

637

638

639





640

#### 641 **Acknowledgments**

642 The field campaign and its associated research, including this work, was primarily funded by the  
643 European Research Council under the Horizon 2020 research and innovation programme  
644 through the ERC Consolidator Grant FRAGMENT (grant agreement No. 773051) and the AXA  
645 Research Fund through the AXA Chair on Sand and Dust Storms at BSC. **CGF** was supported by a  
646 PhD fellowship from the Agència de Gestió d'Ajuts Universitaris i de Recerca (AGAUR) grant  
647 2020\_FI B 00678. **KK** was funded by the Deutsche Forschungsgemeinschaft (DFG, German  
648 Research Foundation) – 264907654; 416816480. **MK** has received funding through the  
649 Helmholtz Association's Initiative and Networking Fund (grant agreement no. VH-NG-1533).

650 We acknowledge the EMIT project, which is supported by the NASA Earth Venture Instrument  
651 program, under the Earth Science Division of the Science Mission Directorate. We thank Dr.  
652 Santiago Beguería from the National Scientific Council of Spain for facilitating a field site in  
653 Zaragoza, Spain, to test our instrumentation and field procedures prior to our campaign in  
654 Morocco. We thank Paul Ginoux for providing high-resolution global dust source maps, which  
655 were very helpful for the identification of the FRAGMENT experimental sites. We thank Prof.  
656 Kamal Taj Eddine from Cady Ayyad University, Marrakesh, Morocco for his invaluable support  
657 and suggestions for the preparation of the field campaign. We thank Prof. Bethany L. Ehlmann  
658 and Dr. Rebecca Greenberger for the help collecting samples, doing infrared in situ spectroscopy  
659 and discussion analysis and to PhD. Abigail M. Keebler for discussion analysis. We thank  
660 Houssine Dakhamat and the crew of Hotel Chez le Pacha in M'hamid El Ghizlane for their support  
661 during the campaign.

#### 662 **Credit authorship contribution statement**

663 **CPG-P** proposed and designed the field campaign with contributions of **AA, KK, MK and XQ**. The  
664 Campaign was implemented by **CPG-P, AA, CGF, AGR, KK, MK, AP, XQ, CR** and **JYD**. The samples  
665 were collected by **CPG-P, AA, AGR, MK and XQ** and analysed by **CB, PC, AGR, CR** and **ZS**.  
666 Spectroscopy was analysed by **RNC**. **AGR** performed the visualization and writing of the original  
667 draft manuscript and **CPG-P** and **XQ** supervised the work. **CPG-P** and **XQ** re-edited the  
668 manuscript and all authors contributed in data discussion, reviewing and manuscript finalization.

669

#### 670 **Declaration of competing interest**

671 Some authors are members of the editorial board of journal ACP. The peer-review process was  
672 guided by an independent editor, and the authors have also no other competing interests to  
673 declare.

674

## 675 **5. References**

- 676 Avila A., Queralt I., Alarcón M.: Mineralogical composition of African dust delivered by red rains  
677 over northeastern Spain. *Journal of Geophysical Research* 102, D18, 21977-21996, 1997.
- 678 Baddock M.C., Ginoux P., Bullard J.E., Gill T.E.: Do MODIS-defined dust sources have a  
679 geomorphological signature?. *Geophys. Res. Lett.*, 43, 2606-2613, 2016.  
680 doi:10.1002/2015GL067327
- 681 Berger E., Bossenbroek L., Beermann A.J., Schäfer R.B., Znari M., Riethmüller S., Sidhu N.,  
682 Kaczmarek N., Benaissa H., Ghamizi M., Plicht S., Salem S.B., El Qorchi F., Naimi M., Leese  
683 F., Frör O.: Social-ecological interactions in the Draa River Basin, southern Morocco:  
684 Towards nature conservation and human well-being using the IPBES framework. *Science of*



- 685 The Total Environment, 769, 144492, ISSN 0048-9697,  
686 <https://doi.org/10.1016/j.scitotenv.2020.144492>, 2021.
- 687 Boose Y., Sierau B., García M.I., Rodríguez S., Alastuey A., Linke C., Schnaiter M., Kupiszewski P.,  
688 Kanji Z.A., Lohmann U.: Ice nucleating particles in the Saharan Air Layer. *Atmospheric*  
689 *Chemistry and Physics*, 16, 14, 9067-9087, 2016.
- 690 Boyd P.W., Jickells T., Law C.S., Blain S., Boyle E.A., Buesseler K.O., Coale K.H., Cullen J.J., De Baar  
691 H.J.W., Follows M., Harvey M., Lancelot C., Levasseur M., Owens N.P.J., Pollard R., Rivkin  
692 R.B., Sarmiento J., Schoemann V., Smetacek V., Takeda S., Tsuda A., Turner S., Watson A.J.:  
693 Mesoscale Iron Enrichment Experiments 1993-2005: Synthesis and Future Directions.  
694 *Science*, 315, 612–617, 2007.
- 695 Bullard J.E., Harrison S.P., Baddock M.C., Drake N., Gill T.E., McTainsh G., Sun Y.: Preferential  
696 dust source: A geomorphological classification designed for use in global dust-cycle models.  
697 *J. of Geoph. Res.*, vol. 116, F04034. doi: 10.1029/2011JF002061, 2011.
- 698 Caquineau S.: Les sources des aérosols sahariens transportés au-dessus de l'Atlantique tropical  
699 nord: Localisation et caractéristiques minéralogiques. Ph.D. thesis, Univ. Paris 12, 1997.
- 700 Caquineau S., Gaudichet A., Gomes L., Magonthier M.C., Chatenet B.: Saharan dust: Clay ratio as  
701 a relevant tracer to assess the origin of soil derived aerosols. *Geophysical Research Letters*,  
702 25, 7, 983-986., 1998.
- 703 Chung F.H.: Quantitative Interpretation of X-Ray Diffraction Patterns of Mixtures. I. Matrix-  
704 Flushing Method for Quantitative Multicomponent Analysis. *Journal of Applied*  
705 *Crystallography*, Vol. 7, 519-525, 1974.
- 706 Claquin T., Schulz M., Balkanski Y.J.: Modeling the mineralogy of atmospheric dust sources.  
707 *Journal Geophysical Research*. 104, D18, 22243-22256, 1999.
- 708 Clark R.N., Swayze G.A., Livo K.E., Kokaly R.F., Sutley S.J., Dalton J.B., McDougal R.R., and Gent  
709 C.A.: Imaging spectroscopy: Earth and planetary remote sensing with the USGS Tetracorder  
710 and expert systems. *Journal of Geophysical Research*, Vol. 108(E12), 5131,  
711 doi:10.1029/2002JE001847, p. 5-1 to 5-44, 2003.
- 712 Clark R.N.: Tetracorder source code on github. [https://github.com/PSI-edu/spectroscopy-](https://github.com/PSI-edu/spectroscopy-tetracorder)  
713 [tetracorder](https://github.com/PSI-edu/spectroscopy-tetracorder). 2023.
- 714 Chatenet B., Marticorena B., Gomes L., Bergametti G.: Assessing the microped size distributions  
715 of desert soils erodible by wind. *Sedimentology*, 43, 5, 901-911, 1996.
- 716 Coudé-Gaussen G., Rognon P., Bergametti G., Gomes L., Strauss B., Gros J. M., Le Coustumer  
717 M.N.: Saharan dust over Fuerteventura Island (Canaries), Chemical and mineralogical  
718 characteristics, air mass trajectories and probable sources. *Geophys. Res.* 92, 9753-9771,  
719 1987.
- 720 De Longueville F., Hountondji Y. C., Henry S., Ozer P.: What do we know about effects of desert  
721 dust on air quality and human health in West Africa compared to other regions?. *Sci. Total*  
722 *Environ.*, 409, 1-8, 2010.
- 723 Di Biagio C., Formenti P., Balkanski Y., Caponi L., Cazaunau M., Pangui E., Journet E., Nowak S.,  
724 Andreae M.O., Kandler K., Saeed T., Piketh S., Seibert D., Williams E., Doussin J.-F.: Complex  
725 refractive indices and single-scattering albedo of global dust aerosols in the shortwave  
726 spectrum and relationship to size and iron content. *Atmos. Chem. Phys.*, 19, 15503-15531,  
727 <https://doi.org/10.5194/acp-19-15503-2019>, 2019.
- 728 Dubief J.: Review of the North African climate with particular emphasis on the production of  
729 aeolian dust in the Sahel zone and in the Sahara, in *Saharan Dust: Mobilization, Transport,*  
730 *Deposition*, edited by C. Morales, 27-48, Wiley, New-York, 1977.
- 731 Echeverría J.C., Morera M.T., Mazkiarán C., Garrido J.J.: Competitive sorption of heavy metal by  
732 soils. Isotherms and fractional factorial experiments. *Environmental Pollution*, 101, 2, 275-  
733 284, ISSN 0269-7491, [https://doi.org/10.1016/S0269-7491\(98\)00038-4](https://doi.org/10.1016/S0269-7491(98)00038-4), 1998.
- 734 Engelbrecht J.P., Moosmüller H., Pincock S., Jayanty R.K.M., Lersch T., Casuccio G., Technical  
735 note: Mineralogical, chemical, morphologica, and optical interrelationships of mineral dust



- 736 re-suspensions. *Atmos. Chem. Phys.*, 16, 10809-10830, doi:10.5194/acp-16-10809-2016,  
737 2016.
- 738 Etzler F.M. and Deanne R.: Particle Size Analysis: A comparison of Various Methods II. Part. Part.  
739 Cyst. *Charact.*, 14, 278-282, 1997.
- 740 FAO-UNESCO: Food & Agriculture Organization-United Nations Educational Scientific, and  
741 Cultural Organization: Guidelines for soil description, 3<sup>rd</sup> edition, Journal FAO & ISRIC,  
742 Rome, 1990.
- 743 Formenti P., Rajot L., Desboeufs K., Caquineau S., Chevaillier S., Nava S., Gaudichet A., Journet  
744 E., Triquet S., Alfaro S., Chiari M., Haywood J., Coe H., Highwood E.: Regional variability of  
745 the composition of mineral dust from western Africa: Results from the AMMA SOPO/DABEX  
746 and DODO field campaigns. *J. Geophys. Res.* 113, D00C13, doi:10.1029/2008JD009903,  
747 2008.
- 748 Ginoux P., Chin M., Tegen I., Prospero J.M., Holben B., Dubovik O., Lin S-J.: Sources and  
749 distributions of dust aerosols simulated with the GOCART model. *Journal of Geophysical  
750 Research: Atmospheres*, 106, D17, 20255.20273, 2001.
- 751 Ginoux P., Prospero J.M., Gill T.E., Hsu N.C., Zhao M.: Global-scale attribution of anthropogenic  
752 and natural dust sources and their emission rates based on MODIS Deep Blue aerosol  
753 products. *Rev. Geophys.*, 50, RG3005, doi:10.1029/2012RG000388, 2012.
- 754 Gobler C.J. and Sañudo-Wilhelmy S.A.: Effects of organic nitrogen, inorganic nutrients, and iron  
755 additions on the growth of phytoplankton and bacteria during a brown tide bloom. *Mar.  
756 Ecol. Prog. Ser.*, 209, 19-34, 2001.
- 757 Gonçalves Ageitos M., Obiso V., Miller R.L., Jorba O., Klose M., Dawson M., Balkanski Y., Perlwitz  
758 J., Basart S., Di Tomaso E., Escribano J., Macchia F., Montané G., Mahowald N., Green R.O.,  
759 Thompson D.R., Pérez García-Pando C.: Modeling dust mineralogical composition:  
760 sensitivity to soil mineralogy atlases and their expected climate impacts. *Atmos. Chem. and  
761 Phys (Preprint)*, 1-51, <https://doi.org/10.5194/egusphere-2022-1414>.
- 762 González-Flórez C., Klose M., Alastuey A., Dupont S., Escribano J., Etyemezian V., Gonzalez-  
763 Romero A., Huang Y., Kandler K., Nikolich G., Panta A., Querol X., Reche C., Yus-Diez J., Pérez  
764 García-Pando C.: Insights into the size resolved dust emission from field measurements in  
765 the Moroccan Sahara. *Atmospheric Chemistry and Physics*, preprint, 2022.
- 766 Gomes L.: Approche géochimique du soulèvement des aérosols à l'interface sol-atmosphère en  
767 zone désertique. Thesis Univ. Paris 7, 251 pp, 1990.
- 768 Goudie A.S. & Middleton N.J.: Desert dust in the global system. Springer, Heidelberg. ISBN 978-  
769 3-540-32355-6, 288 pp, 2006.
- 770 Green R.O., Mahowald N., Ung C., Thompson D.R., Bator L., Bennet M., Zan J.: The earth surface  
771 mineral dust source investigation: an earth science imaging spectroscopy mission. In:  
772 IEEE Aerospace Conference Proceedings. IEEE Computer Society.  
773 <https://doi.org/10.1109/AERO47225.2020.9172731>. 2020.
- 774 Harrison A.D., Lever K., Sanchez-Marroquin A., Holden M.A., Whale T.F., Tarn M.D., McQuaid  
775 J.B., Murray B.J., The ice-nucleating ability of quartz immersed in water and its  
776 atmospheric importance compared to K-feldspar. *Atmos. Chem. Phys.*, 19, 11343–  
777 11361, 2019.
- 778 Horváth B., Opara-Nadi O., Beese F.: A simple method for measuring the carbonate content of  
779 soils. *SSSA*, 69 n° 4. 593-604, 2005.
- 780 Ito A. & Wagai R.: Global distribution of clay-size minerals on land surface for biogeochemical  
781 and climatological studies. *Scientific Data*, 4:170103, 2017. DOI: 10.1038/sdata.2017.103.
- 782 Journet E., Balkanski Y., Harrison S.P.: A new data set of soil mineralogy for dust-cycle modeling.  
783 *Atmos. Chem. Phys.*, 14, 8, 3801-3816, 2014.
- 784 Karanasiou A., Moreno N., Moreno T., Viana M., de Leeuw F., Querol X.: Health effects from  
785 Sahara dust episodes in Europe: Literature review and research gaps. *Environ. Int.* 47, 107–  
786 14, 2012.



- 787 Klose M., Jorba O., Gonçalves Ageitos M., Escribano J., Dawson M.L., Obiso V., Di Tomaso E.,  
788 Basart S., Montané Pinto G., Macchia F., Ginoux P., Guerschman J., Prigent C., Huang Y., Kok  
789 J.F., Miller R.L., and Pérez García-Pando C.: Mineral dust cycle in the Multiscale Online  
790 Nonhydrostatic Atmosphere Chemistry model (MONARCH) Version 2.0. *Geosci. Model*  
791 *Dev.*, 14, 6403–6444, <https://doi.org/10.5194/gmd-14-6403-2021>, 2021.
- 792 Kok J.F., Adebisi A.A., Albani S., Balkanski Y., Checa-Garcia R., Chin M., Colarco P.R., Hamilton  
793 D.S., Huang Y., Ito A., Klose M., Li L., Mahowald N.M., Miller R.L., Obiso V., Pérez García-  
794 Pando C., Rocha-Lima A., Wan J.S.: Contribution of the world's main dust source regions to  
795 the global cycle of desert dust. *Atmos. Chem. Phys.*, 21, 8169–8193, 2021.  
796 <https://doi.org/10.5194/acp-21-8169-2021>
- 797 Li L., Mahowald N., Miller R., Pérez García-Pando C., Klose M., Hamilton D., Gonçalves Ageitos  
798 M., Ginoux P., Balkanski Y., Green R., Kalashnikova O., Kok J., Obiso V., Paynter D., and  
799 Thompson D.: Quantifying the range of the dust direct radiative effect due to source  
800 mineralogy uncertainty. *Atmospheric Chemistry and Physics*. 21, 3973–4005,  
801 <https://doi.org/10.5194/acp-21-3973-2021>, 2021.
- 802 Mebius L.J.: A rapid method for the determination of organic carbon in soil. *Analytica Chimica*  
803 *Acta*, 22, 120–124, 1960.
- 804 Middleton N.J.: Desert dust hazards: A global review. *Aeolian research*, 24, 53–63, 2017.
- 805 Molinaroli E., Guerzoni S., Rampazzo G.: Contribution of Saharan dust to the central  
806 Mediterranean basin. *Geological Society of America, Special paper*, 284, 303–312, 1993.
- 807 Monteiro A., Basart S., Kazadzia S., Votsis A., Gkikas A., Vandenbussche S., Tobias A., Gama C.,  
808 Pérez García-Pando C., Terradellas E., Notas G., Middleton N., Kushta J., Amiridis V.,  
809 Lagouvardos K., Kosmopoulos P., Kotroni V., Kanakidou M., Mihalopoulos N., Kalivitis N.,  
810 Dagsson-Waldhauserová P., El-Askary H., Sievers K., Giannaros T., Mona L., Hirtl M.,  
811 Skomorowski P., Virtanen T.H., Christoudias T., Di Mauro B., Tripetta S., Kutuzov S.,  
812 Meinander O., Nickovic S.: Multi-sectorial impact assessment of an extreme African dust  
813 episode in the Eastern Mediterranean in March 2018. *Science of the Total Environment*,  
814 843, 156861, 2022.
- 815 Nelson D.W. & Sommers L.E.: A rapid and accurate method for estimating organic carbon in soil.  
816 *Proceedings of the Indiana Academy of Science*, 84, 456–462, 1975.
- 817 Nickovic S., Vukovic A., Vujadinovic M., Djurdjevic V., Pejanovic G.: Technical Note: High-  
818 resolution mineralogical database of dust-productive soils for atmospheric dust modelling.  
819 *Atmos. Chem. Phys.*, 12, 2, 845–855, 2012.
- 820 Panta A., Kandler K., Alastuey A., González-Flórez C., González-Romero A., Klose M., Querol X.,  
821 Reche C., Yus-Díez J., Pérez García-Pando C.: Insights into the single particle composition,  
822 size, mixing state and aspect ratio of freshly emitted mineral dust from field measurements  
823 in the Moroccan Sahara using electron microscopy. *Atmospheric Chemistry and Physics*,  
824 preprint, 2022.
- 825 Pérez C., Hausteijn K., Janjic Z., Jorba O., Huneus N., Baldasano J.M., Black T., Basart S., Nickovic  
826 S., Miller R.L., Perlwitz J. P., Schulz M., and Thomson M.: Atmospheric dust modeling from  
827 meso to global scales with the online NMMB/BSC-Dust model-Part 1: Model description,  
828 annual simulations and evaluation. *Atmos. Chem. Phys.*, 11, 13001–13027,  
829 <https://doi.org/10.5194/acp-11-13001-2011>, 2011.
- 830 Pérez García-Pando C., Stanton M.C., Diggle P.J., Trzaska S., Miller R.L., Perlwitz J.P., Baldasano  
831 J.M., Cuevas E., Ceccato P., Yaka P., Thomson M.C.: Soil dust aerosols and wind as predictors  
832 of seasonal meningitis incidence in Niger. *Environ. Health Perspect.* 122, 7679–686, 2014.
- 833 Perlwitz J.P., Pérez García-Pando C., and Miller R.L.: Predicting the mineral composition of dust  
834 aerosols – Part 1: Representing key processes. *Atmos. Chem. Phys.* 15, 11593–11627,  
835 <https://doi.org/10.5194/acp-15-11593-2015>, 2015.
- 836 Prospero J.M., Ginoux P., Torres O., Nicholson S.E., Gill T.E.: Environmental characterization of  
837 global sources of atmospheric soil dust identified with the Nimbus 7 Total Ozone Mapping



- 838 Spectrometer (TOMS) absorbing aerosol product. *Rev. Geophys.*, 40, 1, 1002,  
839 doi:10.1029/2000RG000095, 2002.
- 840 Pye K. & Tsoar H.: The mechanics and geological implications of dust transport and deposition  
841 in deserts with particular reference to loess formation and dune sand diagenesis in the  
842 northern Negev, Israel. *Geol. Soc. Of London Publ.* 139-156, doi:  
843 10.1144/GSL.SP.1987.035.01.10, 2015.
- 844 Querol X.: The Occurrence and Distribution of Trace Elements in the Teruel Mining District Coals  
845 and their Behaviour during Coal Combustion. European Coal and Steel Community Project  
846 7220/ED/014, 1993.
- 847 Querol X., Whateley M.K.G., Fernandez-Turiel J.L., Tuncali E.: Geological controls on the  
848 mineralogy and geochemistry of the Bepazari lignite, Central Anatolia, Turkey. *Int. J. Coal.*  
849 *Geol.*, 33:255–271, 1997.
- 850 Querol X., Tobías A., Pérez N., Karanasiou A., Amato F., Stafoggia M., Pérez García-Pando C.,  
851 Ginoux P., Forastiere F., Gumy S., Mudu P., Alastuey A.: Monitoring the impact of desert  
852 dust outbreaks for air quality for health studies. *Env. International*, 130, 104867, 2019.
- 853 Reynolds R.L., Cattle S.R., Moskowitz B.M., Goldstein H.L., Yauk K., Flagg C.B., Berquó T.S., Kokaly  
854 R.F., Morman S., Breit G.N. : Iron oxide minerals in dust of the Red Dawn event in eastern  
855 Australia, September 2009. *Aeolian Research*, 15, 1-13, 2014.
- 856 Sabre M.: Étude dynamique du processus d'Émission de poussières désertiques: impact sur le  
857 fractionnement chimique entre sol et aérosol. Thesis Univ. Paris 7, 170 pp, 1997.
- 858 Scanza R.A., Mahowald N., Ghan S., Zender C.S., Kok J.F., Liu X., Zhang Y., Albani S.: Modelling  
859 dust as component minerals in the Community Atmosphere Model: development of  
860 framework and impact on radiative forcing. *Atmos. Chem. Phys.*, 15, 537–561, 2015.
- 861 Scheuvsens D., Schütz L., Kandler K., Ebert M., Weinbruch S.: Bulk composition of northern  
862 African dust and its source sediments - A compilation. *Earth-Science Rev.*, 116, 1, 170-194,  
863 2013.
- 864 Schütz L. & Seibert M.: Mineral aerosols and source identification. *Journal of Aerosol Science* 18,  
865 1, 1-10, 1987.
- 866 Shao Y., Ishizuka M., Mikami M., Leys J.F.: Parameterization of size-resolved dust emission and  
867 validation with measurements. *J. Geophys. Res.*, 116, D08203. doi:10.1029/2010JD014527,  
868 2011.
- 869 Shen Z., Caquineau S., Cao J., Zhang X., Hana Y., Gaudichet A., Gomes L.: Mineralogical  
870 characteristics of soil dust from source regions in northern China. *Particuology* 7, 507-512,  
871 2009.
- 872 Shi Z.B., Krom M.D., Bonneville S.: Formation of Iron Nanoparticles and Increase in Iron  
873 Reactivity in Mineral Dust during Simulated Cloud Processing. *Environ. Sci. Technol.* 43,  
874 6592-6596, 2009.
- 875 Shi Z.B., Krom M.D., Jickells T.D., Bonneville S., Carslaw K. S., Mihalopoulos N., Baker A. R.,  
876 Benning L. G.: Impacts on iron solubility in the mineral dust by processes in the source  
877 region and the atmosphere: A review. *Aeolian Research*, 5, 21-42.  
878 <https://doi.org/10.1016/j.aeolia.2012.03.001>, 2012.
- 879 Sokolik I.N. & Toon O.B.: Incorporation of mineralogical composition into models of the radiative  
880 properties of mineral aerosol from UV to IR wavelengths. *J. Geophys. Res.*, 104, 9423-9444,  
881 1999.
- 882 Sperazza M., Moore J.N., Hendrix M.: High-Resolution particle size analysis of naturally occurring  
883 very fine-grained sediment through laser diffractometry. *J. Sediment. Res.*, 74(5):736-743,  
884 2004.
- 885 Stout J.E., Lee J.A.: Indirect evidence of wind erosion trends on the Southern High Plains of North  
886 America. *Journal of Arid Environments*, 55, 1, 43-61, 2003.
- 887 Sullivan R.C., Guazzotti S.A., Sodeman D.A., Tang Y., Carmichael G.R., Prather K.A.: Mineral dust  
888 is a sink for chlorine in the marine boundary layer. *Atmos. Environ.* 41, 7166-7179, 2007.



- 889 Tegen I., Harrison S.P., Kohfeld K., Prentice I.C., Coe M., Heimann M.: Impact of vegetation and  
890 preferential source areas on global dust aerosol: Results from a model study. *Journal of*  
891 *Geophysical Research: Atmospheres*, 107, D21, AAC 14-a-AAC 14-27, 2002.
- 892 Tegen I., Hollrig P., Chin m., Fung I., Jacob D., Penner J.: Contribution of different aerosol  
893 extinction optical thickness: Estimates from model results. *Journal of Geophysical Research:*  
894 *Atmospheres*, 102, D21, 23895-23915, 1997.
- 895 Tegen I., Fung I.: Modeling of mineral dust in the atmosphere: Sources, transport, and optical  
896 thickness, *J. Geophys. Res.*, 99, 22897-22914, 1994.
- 897 Thorez, J.: *Practical Identification of clay minerals*. G. Lellote, Dison (Belgique), 90pp, 1976.
- 898 Urquhart L. C.: *Civil Engineering Handbook*, McGraw Hill, New York, 1959
- 899 Valentin C. & Bresson L.M.: Morphology, génesis and classification of Surface crusts in loamy  
900 and Sandy soils. *Geoderma*, 55, 225-245, 1992.
- 901 Van der Watt H.v.H. & Valentin C.: Soil crusting: The African view. In Summer, M.E., Stewart, B.A.  
902 (Eds.), *Soil Crusting, Chemical and Physical Processes*. CRC Press, Boca Raton, 301-338,  
903 1992.
- 904 Walkley A. & Black I.A.: An examination of Degtjareff method for determining soil organic matter  
905 and a proposed modification of the chromic acid titration method. *Soil Science*, 37, 29-37,  
906 1934.
- 907 Weaver C.J., Ginoux P., Hsu N.C., Chou M.-D., Joiner J.: Radiative forcing of Saharan dust:  
908 GOCART model simulations compared with ERBE data. *J. Atmos. Sci.*, 59:736–747, 2002.
- 909 Wentworth C.K.: A scale of grade and class terms for clastic sediments. *The journal of geology*,  
910 30, 5, 377-392, doi:10.1086/622910, 1922.
- 911 Yus-Díez J., Pandolfi M., González-Flórez C., Escribano J., Gonzalez-Romero A., Ivancic M., Rigler  
912 M., Klose M., Kandler K., Panta A., Querol X., Reche C., Pérez García-Pando C., and Alastuey,  
913 A.: Quantifying variations in multi-wavelength optical properties of freshly-emitted Saharan  
914 dust from the Lower Drâa Valley, Moroccan Sahara, in prep
- 915 Zender C.S., Newman D., Torres O.: Spatial heterogeneity in aeolian erodibility: Uniform,  
916 topographic, geomorphic, and hydrologic hypotheses. *Journal of Geophysical Research-*  
917 *Atmospheres* 108, 4543, 2003.
- 918 Zender C.S., Miller R.L., Tegen I.: Quantifying mineral dust mass budgets: Terminology,  
919 constraints, and current estimates. *Eos, Transactions American Geophysical Union*. 85, 48,  
920 509-512, <https://doi.org/10.1029/2004EO480002>, 2004
- 921  
922  
923  
924  
925  
926  
927  
928  
929  
930  
931  
932  
933  
934  
935  
936





937 **Figure captions**

938 **Figure 1.** a) Location of the study area (exact location of data measurement “star”: 29°49’30”N,  
939 5°52’25”W), near M’Hamid el Ghizlane, into the Drâa basin in S Morocco. Base layer from  
940 world imagery of Google Earth Pro v:7.3.6.9345. b) Frequency of occurrence (%) of dust  
941 optical depth above 0.2 in September, October and November between 2003 and 2016  
942 derived from MODIS Deep Blue. c) EMIT scenes  
943 emit20220903t082303\_o24606\_s001\_l2a\_rfl\_b0106\_v01 and  
944 emit20230206t101334\_o03707\_s000\_l2a\_rfl\_b0106\_v01 at 60 meters per pixel show the  
945 diversity of Fe<sup>2+</sup> and Fe<sup>3+</sup> bearing minerals (left) and the EMIT 8 phyllosilicates, carbonates,  
946 and sulphates (right). The mineral maps were produced by tetracorder 5.27c1 (Clark, 2023).  
947 There is some mapped mineralogy difference at the scene boundaries, possibly due to the  
948 changing viewing geometry, and variation in atmospheric removal between the two scenes.  
949 Cirrus clouds in the scene on the right may also be impacting derived mineralogy.

950 **Figure 2.** Images of samples collected during a field campaign near M’Hamid el Ghizlane, into  
951 the Draa Basin, S Morocco.

952 **Figure 3.** Median minimally and fully dispersed PSDs of crusts, sediments, paved sediments and  
953 dunes. (a) MDPSDs and (b) FDPDs combined from crust, sediment and paved sediment  
954 samples; (c) and (d) are MDPSDs and FDPDs for dune samples; (e) and (f) are MDPSDs and  
955 FDPDs differentiated by type of sample.

956 **Figure 4.** Boxplot of median particle size diameters in  $\mu\text{m}$  including both fully and minimally  
957 dispersed analysis (a) for all samples combined excluding dunes and (b) for dune samples  
958 only. Also particle size diameter in  $\mu\text{m}$  for crusts, sediment and paved sediment for (c)  
959 minimally dispersed and (d) fully dispersed results. Means median diameters for each  
960 sediment type are shown with crosses.

961 **Figure 5.** Spatial variation map with crust fully dispersed mean median particle diameter.

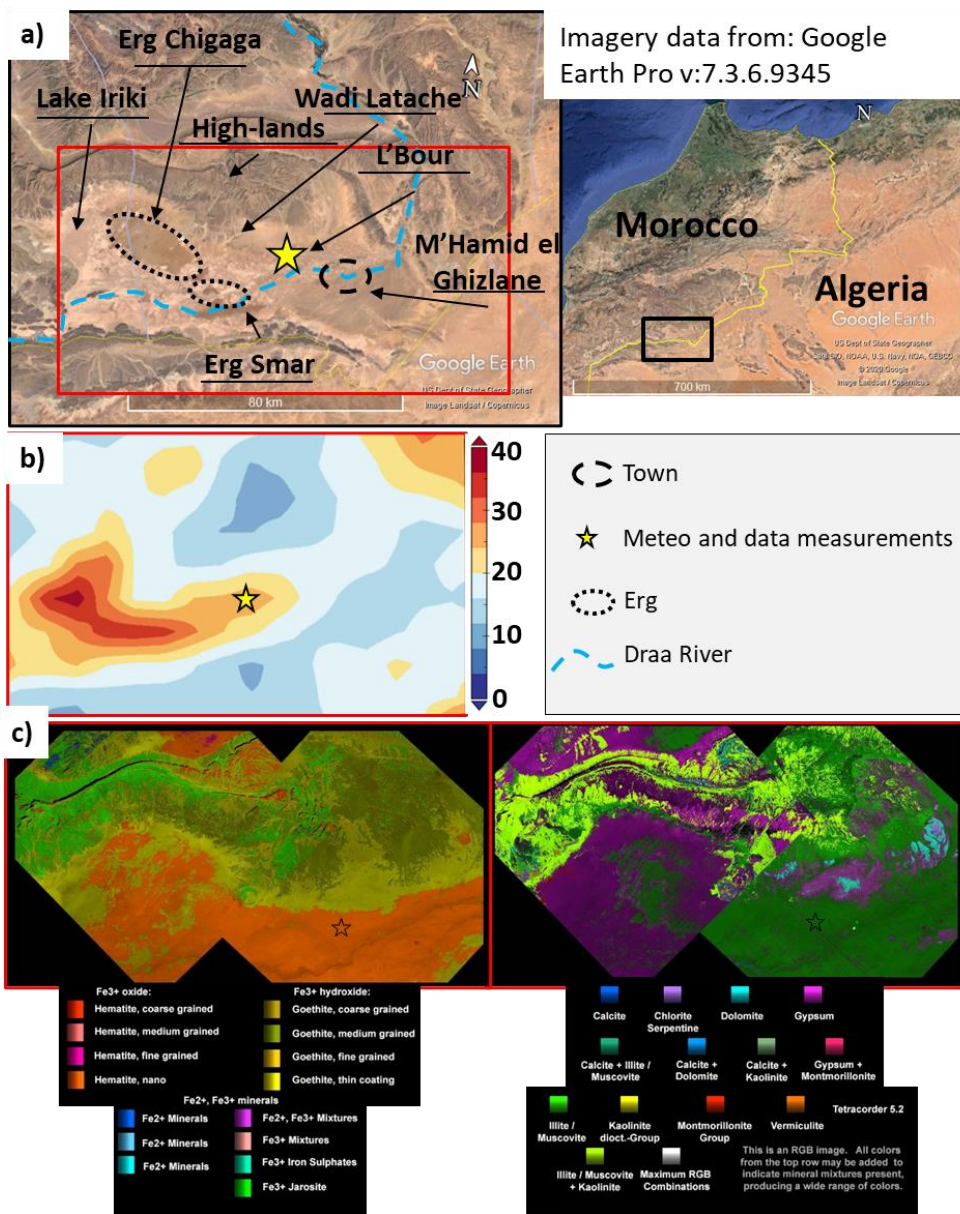
962 **Figure 6.** Mean mineral group content of dune, crust, paved sediment and sediment samples,  
963 and also at Erg Smar, L’Bour and High-lands. Solid lines mark the mean content of all the  
964 samples (excluding dune samples). The dashed line divides between type and location of  
965 the samples.

966 **Figure 7.** Schematic model of sedimentation and deposition processes in our study site from  
967 high-lands to low-lands for a) crusts and for b) paved sediments.

968 **Figure 8.** Dust emission conceptual model integrating particle size distributions and mineralogy  
969 of dust source sediments. a) Refers to the conceptual thickness and particle size  
970 distributions along the basin, b) to the particle size distribution and segregation of  
971 mineralogy and c) to the dust emission quantity expected depending on the place in the  
972 basin.

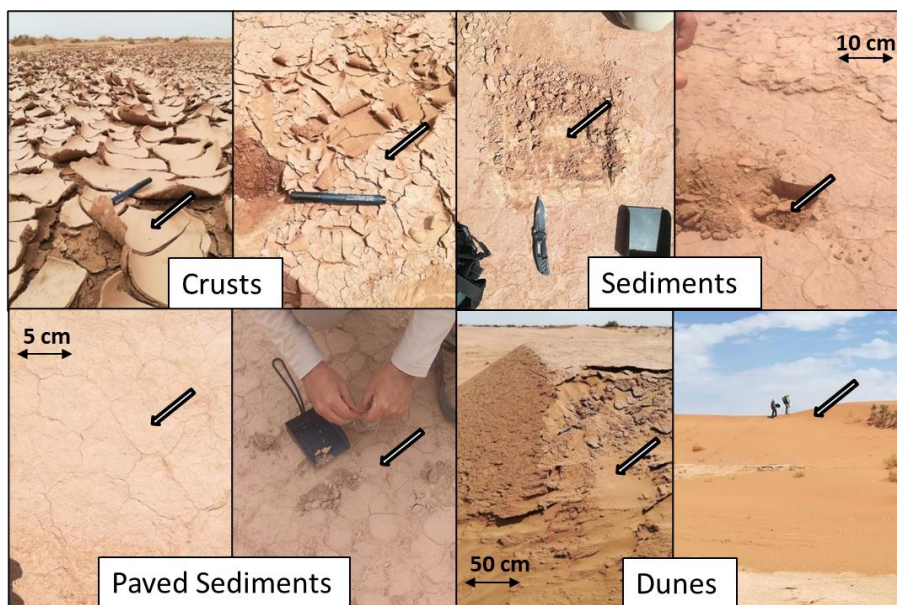
973  
974  
975



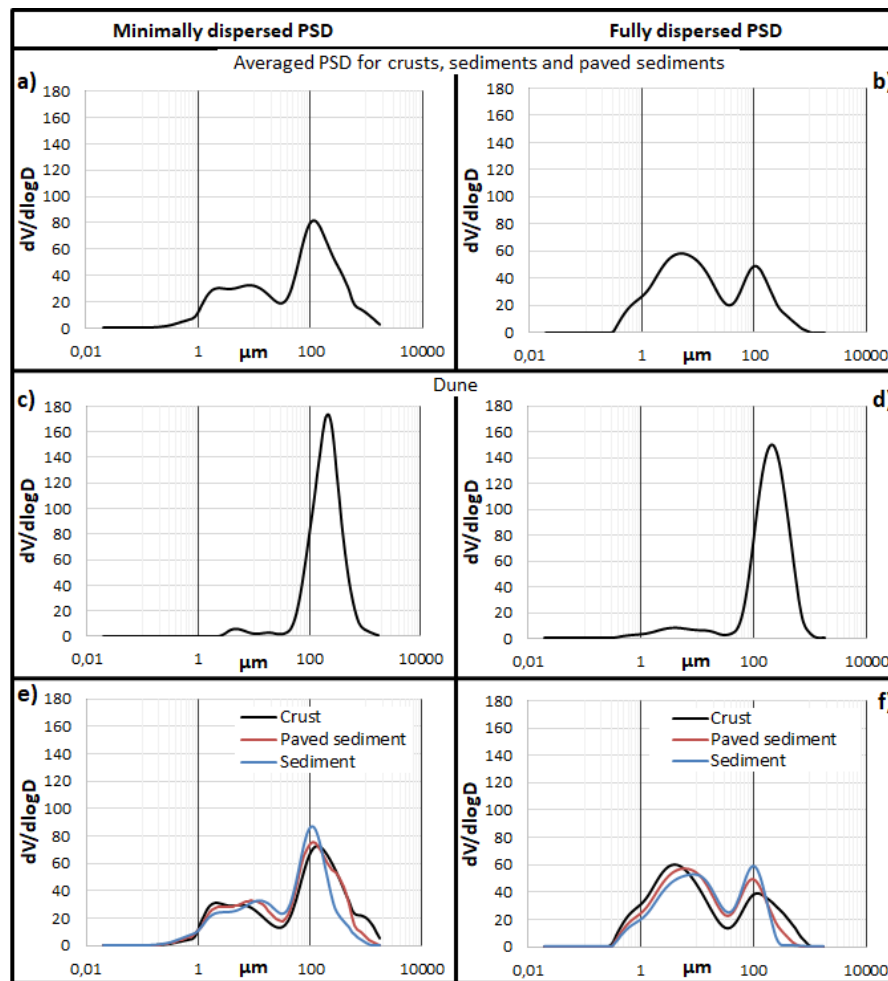


976  
977  
978  
979  
980  
981  
982

Figure 1.

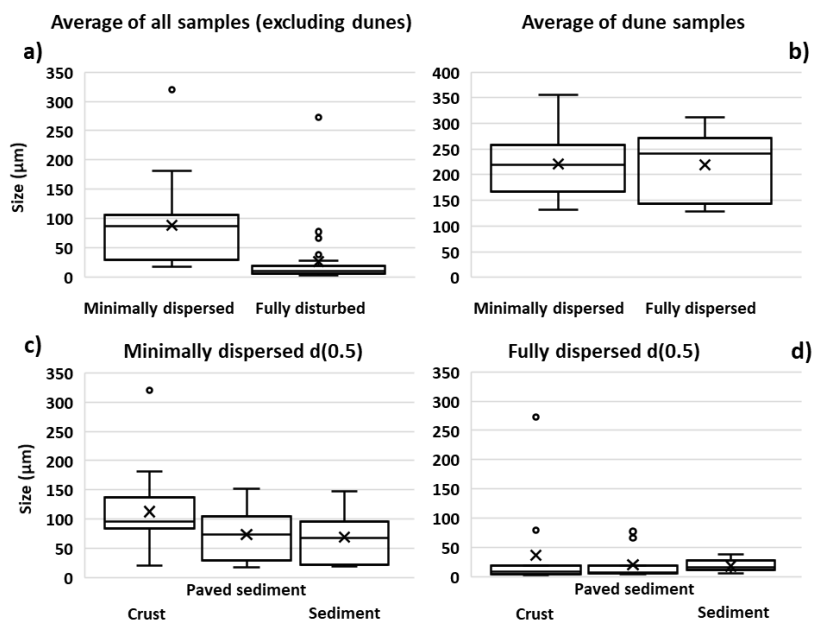


983  
984 Figure 2.  
985  
986  
987  
988  
989  
990  
991  
992  
993  
994  
995  
996  
997  
998  
999  
1000  
1001  
1002  
1003  
1004  
1005  
1006  
1007  
1008  
1009  
1010



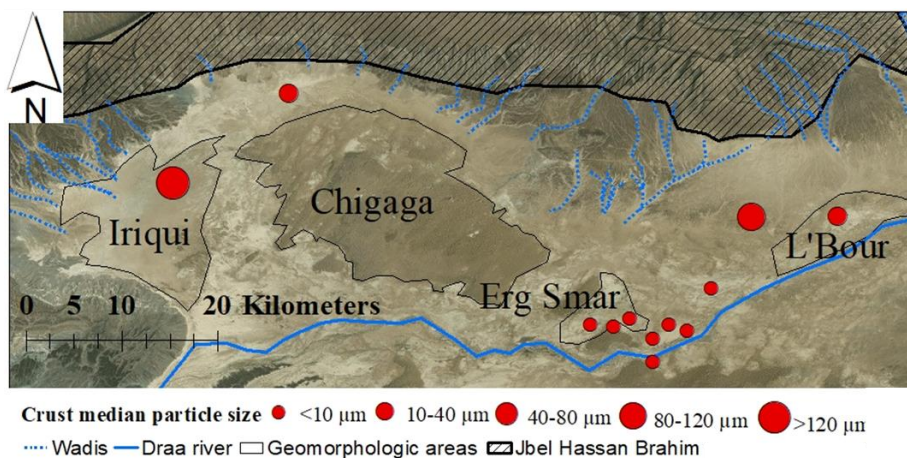
1011  
1012  
1013  
1014  
1015  
1016  
1017  
1018  
1019  
1020  
1021  
1022  
1023  
1024

Figure 3.



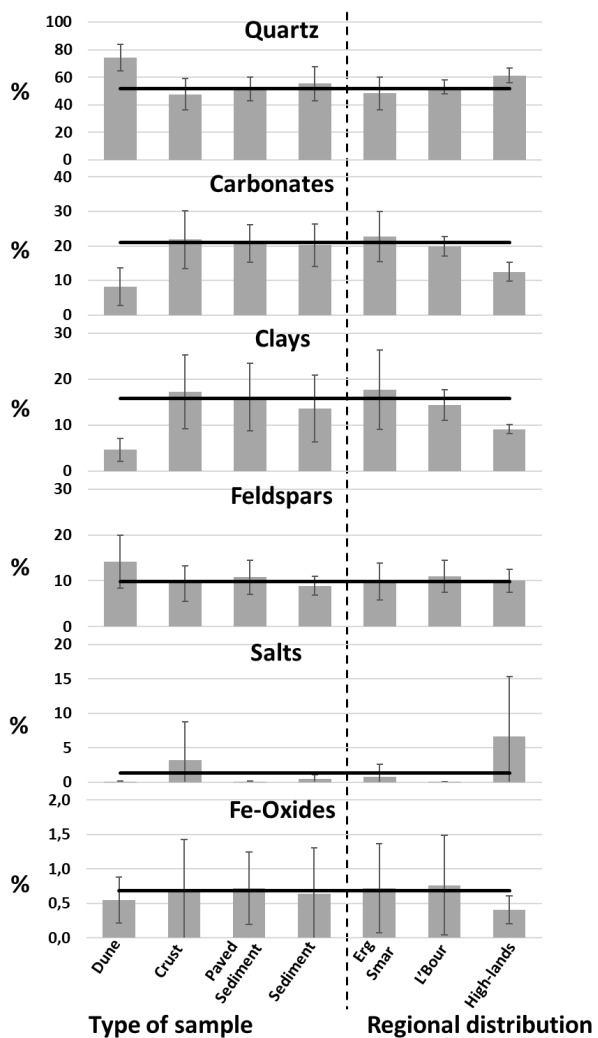
1025  
1026  
1027  
1028  
1029

Figure 4.



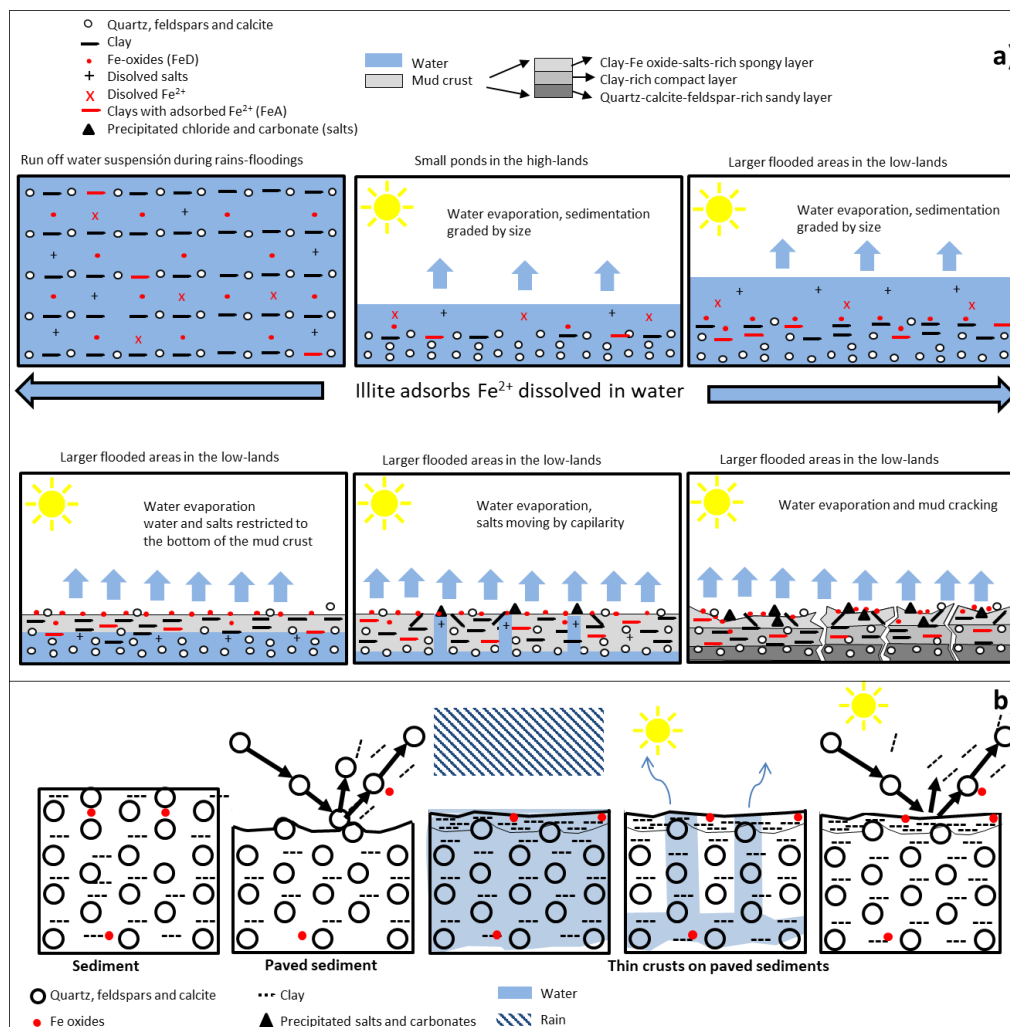
1030  
1031  
1032  
1033  
1034

Figure 5.



1035  
1036 Figure 6.  
1037  
1038  
1039  
1040  
1041  
1042  
1043  
1044  
1045



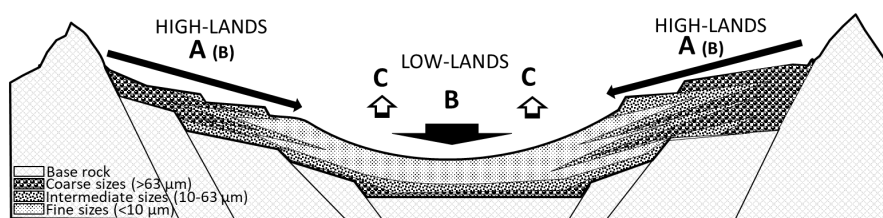


1046  
1047  
1048  
1049  
1050  
1051  
1052  
1053  
1054  
1055  
1056  
1057  
1058  
1059  
1060  
1061

Figure 7.

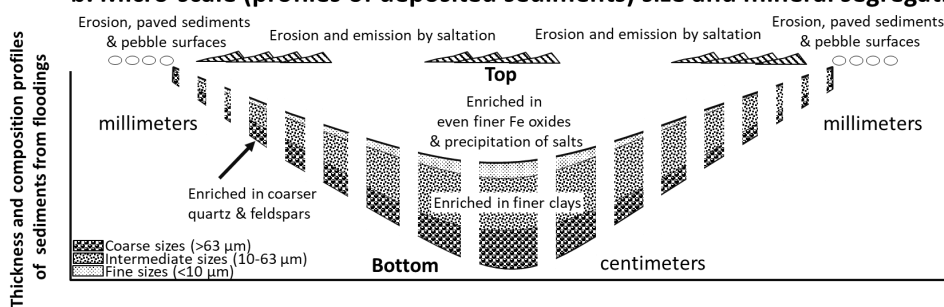


**a. Macro-scale (basin) size and mineral segregation of sediments**

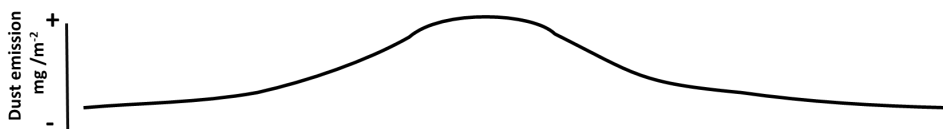


A: Washout, erosion and sporadic flooding with deposition of coarser sediments enriched in quartz and feldspars  
 B: Flooding and deposition of finer sediments enriched in clays and Fe oxides  
 C: Evaporation and deposition of fine clays and readily exchangeable Fe oxide, salt crystallization in upper layers

**b. Micro-scale (profiles of deposited sediments) size and mineral segregation**



**c. Higher dust emissions (high Fe oxide and clay) in low-lands with thicker & finer deposited sediments**



**a+b+c= Emitted dust might be markedly enriched in clays and Fe oxides compared to the parent sediments/soils**

1062  
 1063  
 1064  
 1065  
 1066  
 1067  
 1068  
 1069

Figure 8.





Table 1. Full range, <63µm and >63 to 2000 µm mean diameter, standard deviation, min., max. and for Minimally dispersed particle size distribution and fully dispersed particle size distribution.

Surface Type	Location	Nº of samples	MDPSD		
			Full range	≤ 63 µm	>63 to 2000 µm
Mean of medians ± sd [Min,Max]					
Dunes	Mean	12	221 ± 64 [132,355]	32 ± 9.3 [20,46]	252 ± 65 [142,364]
	High-Land	3	212 ± 27 [195,243]	45 ± 1.3 [44,46]	259 ± 22 [243,284]
	Erg Smar	4	286 ± 49 [244,355]	32 ± 8.1 [25,41]	295 ± 52 [238,364]
	L'Bour	5	174 ± 45 [132,244]	27 ± 7.4 [20,36]	214 ± 76 [142,332]
Crusts	Mean	12	113 ± 79 [20, 320]	15 ± 3.7 [7.7,19]	308 ± 146 [146,635]
	High-Land	3	94 ± 5 [89,99]	18 ± 1.1 [17,19]	219 ± 28 [187,238]
	Erg Smar	8	131 ± 89 [21,320]	13 ± 3.4 [7.7,17]	362 ± 151 [193,635]
	L'Bour	1	20 ± NA [NA,NA]	15 ± NA [NA,NA]	146 ± NA [NA,NA]
Paved Sediments	Mean	11	74 ± 48 [19,152]	17 ± 6.7 [11,33]	237 ± 71 [146,387]
	High-Land	0	NA	NA	NA
	Erg Smar	8	68 ± 46 [19, 148]	17 ± 7.0 [11,33]	240 ± 43 [167,320]
	L'Bour	3	90 ± 61 [29,148]	18 ± 7.1 [13,26]	230 ± 137 [146,387]
Sediments	Mean	7	70 ± 45 [20,147]	18 ± 5.1 [15,29]	175 ± 58 [129,302]
	High-Land	1	97 ± NA [NA,NA]	18 ± NA [NA,NA]	149 ± NA [NA,NA]
	Erg Smar	2	115 ± 45 [83,147]	22 ± 11 [15,29]	229 ± 104 [155,302]
	L'Bour	4	40 ± 23 [20,68]	17 ± 0.79 [16,17]	155 ± 21 [129,178]
FDPSD					
Dunes	Mean	12	219 ± 70 [128,312]	24 ± 13 [9.0,46]	247 ± 72 [145,355]
	High-Land	3	250 ± 73 [169,312]	41 ± 6.8 [33,46]	290 ± 77 [205,355]
	Erg Smar	4	263 ± 32 [239,308]	20 ± 6.2 [13,25]	279 ± 33 [238,319]
	L'Bour	5	166 ± 61 [128,272]	16 ± 7.5 [9.0,26]	195 ± 68 [145,310]
Crusts	Mean	12	37 ± 77 [2.7,272]	9.8 ± 3.6 [3.6,16]	196 ± 76 [119,389]
	High-Land	3	124 ± 132 [20,272]	13 ± 1.1 [12,14]	251 ± 121 [162,389]
	Erg Smar	8	7 ± 3 [2.7,10]	7.9 ± 2.5 [3.6,11]	183 ± 44 [130,236]
	L'Bour	1	17 ± NA [NA,NA]	16 ± NA [NA,NA]	119 ± NA [NA,NA]
Paved Sediments	Mean	11	21 ± 26 [2.3,78]	13 ± 4.8 [8.2,21]	157 ± 36 [120,221]
	High-Land	0	NA	NA	NA
	Erg Smar	8	18 ± 24 [5.9,78]	12 ± 4.6 [8.2,21]	169 ± 34 [129,221]
	L'Bour	3	29 ± 33 [5.3,67]	14 ± 6.0 [8.3,20]	122 ± 2.2 [120,124]
Sediments	Mean	7	19 ± 11 [5.8,39]	14 ± 3.9 [7.7,19]	128 ± 9.6 [117,144]
	High-Land	1	12 ± NA [NA,NA]	9.9 ± NA [NA,NA]	133 ± NA [NA,NA]
	Erg Smar	2	22 ± 23 [5.8,39]	13 ± 8.1 [7.7,19]	126 ± 13 [117,135]
	L'Bour	4	19 ± 6.3 [13,28]	15 ± 1.3 [13,17]	128 ± 11 [122,144]



Table 2. Mineral results from samples and type of sample. In type of samples, C: Crust, PS: Paved sediment, S: Sediment, D: Dune. In Loc (Location), ES: Erg Smar, LB: L’ Bour, HL: High-lands. Sme: Smectite, Mca: Mica/illite, Kln: Kaolinite, Chl: Chlorite, Plg: Palygorskite, Qtz: Quartz, Cal: Calcite, Dol: Dolomite, Hl: Halite, Gp: Gypsum, Mc: Microcline, Ab: Albite and anorthite, Hem: Hematite, Gt: Goethite. <0.1 indicates below limit of detection.

Type	Loc	Qtz	Feldspars		Carbonates		Clays					Salts		Iron Oxides	
			Mc	Ab	Cal	Dol	Sme	Mca	Kln	Chl	Plg	Hl	Gp	Hem	Gt
C	ES	55	2,6	4,8	20	3,3	<0.1	11	<0.1	1,2	<0.1	<0.1	<0.1	1,2	<0.1
C	ES	57	2,7	3,1	20	3,4	<0.1	5,2	<0.1	0,78	0,26	7,2	<0.1	0,87	<0.1
C	ES	36	2,2	10	21	2,7	<0.1	15	10,0	1,4	<0.1	<0.1	0,20	1,2	<0.1
C	ES	32	1,7	3,3	29	3,4	<0.1	10	17	2,2	0,20	<0.1	<0.1	0,24	1,3
C	ES	38	3,7	4,7	18	6,2	<0.1	14	9,0	1,3	0,14	3,5	0,14	0,95	<0.1
C	ES	50	5,5	5,5	14	2,8	<0.1	12	7,9	1,3	<0.1	<0.1	<0.1	0,21	0,85
C	LB	50	13	5,1	12	3,6	<0.1	8,1	5,7	0,46	<0.1	<0.1	<0.1	0,92	<0.1
C	HL	63	6,9	6,8	12	2,2	<0.1	4,5	3,9	0,19	<0.1	<0.1	<0.1	0,11	0,40
C	ES	45	3,7	3,2	26	3,2	<0.1	11	5,4	1,8	0,21	<0.1	<0.1	<0.1	0,18
C	ES	30	2,6	3,4	35	2,5	0,57	8,8	14	1,4	1,5	0,14	<0.1	0,14	0,17
C	HL	60	3,7	5,5	11	0,98	<0.1	5,7	3,4	0,97	0,19	8,1	0,21	0,41	0,60
C	HL	54	4,7	3,9	7,1	1,79	<0.1	5,4	3,3	0,60	<0.1	16	2,0	0,22	0,65
S	ES	35	1,8	4,1	24	5,6	<0.1	17	8,3	2,2	<0.1	1,1	0,19	1,1	<0.1
S	ES	67	6,6	5,1	10	2,1	<0.1	3,0	3,6	0,64	<0.1	1,1	<0.1	0,42	0,23
S	LB	51	4,6	7,9	15	4,2	<0.1	8,9	6,6	0,89	<0.1	<0.1	<0.1	<0.1	0,82
S	LB	57	2,7	7,8	16	3,8	<0.1	9,6	1,9	0,49	<0.1	<0.1	<0.1	0,93	<0.1
S	LB	57	3,4	5,4	18	3,2	<0.1	6,5	3,5	2,1	<0.1	<0.1	<0.1	0,33	0,60
S	HL	67	3,2	5,3	13	1,7	0,13	4,3	3,2	0,20	0,20	<0.1	<0.1	<0.1	0,90
S	LB	51	3,4	5,1	21	3,3	<0.1	8,5	4,5	2,2	0,15	<0.1	<0.1	0,66	0,50
PS	ES	44	3,0	5,7	15	3,1	<0.1	16	11	1,5	<0.1	<0.1	<0.1	0,35	0,64
PS	ES	44	2,2	5,4	22	4,7	<0.1	13	6,8	0,54	<0.1	<0.1	<0.1	1,1	<0.1
PS	ES	55	2,3	5,4	24	3,6	<0.1	7,8	0,84	0,28	0,17	<0.1	<0.1	0,98	<0.1
PS	ES	40	5,3	4,7	20	4,3	<0.1	13	10	1,1	<0.1	<0.1	0,29	0,77	0,23
PS	ES	67	8,8	8,7	8,9	1,8	<0.1	3,1	0,38	0,30	<0.1	<0.1	<0.1	0,30	0,29
PS	LB	48	5,5	4,0	16	4,3	<0.1	11	8,7	1,3	0,13	<0.1	<0.1	1,1	<0.1
PS	ES	61	3,5	6,3	12	3,6	<0.1	7,9	3,6	0,78	0,16	<0.1	<0.1	0,41	0,33
PS	ES	46	9,1	9,0	14	3,3	0,29	6,6	8,8	1,0	0,42	<0.1	<0.1	0,42	0,69
PS	ES	48	2,3	7,3	22	3,7	<0.1	8,1	6,3	1,3	<0.1	<0.1	0,16	0,17	1,1
PS	LB	61	4,0	8,1	13	3,3	<0.1	4,3	4,2	1,2	<0.1	<0.1	<0.1	0,16	0,64
PS	LB	51	3,6	4,4	22	3,1	<0.1	8,5	4,3	2,0	0,17	<0.1	<0.1	0,68	0,53
D	ES	80	7,1	7,0	3,1	0,69	<0.1	1,4	<0.1	<0.1	<0.1	<0.1	<0.1	<0.1	0,38
D	ES	65	14	8,3	4,1	0,90	<0.1	4,8	1,9	<0.1	<0.1	<0.1	<0.1	<0.1	0,37
D	LB	73	7,0	11	6,6	0,31	<0.1	1,2	0,19	0,23	<0.1	<0.1	<0.1	0,11	0,32
D	ES	89	2,5	3,0	2,0	<0.1	<0.1	0,69	1,4	<0.1	<0.1	<0.1	<0.1	0,45	0,65
D	ES	65	12	5,4	11	1,3	0,13	2,7	2,1	0,38	<0.1	<0.1	<0.1	0,12	0,32
D	LB	64	5,0	6,8	10	5,0	<0.1	3,1	4,3	0,50	<0.1	<0.1	<0.1	<0.1	0,61
D	LB	76	4,1	6,7	6,6	0,52	<0.1	2,6	2,2	0,21	<0.1	0,28	<0.1	0,25	0,21
D	LB	77	3,9	6,7	7,5	0,53	0,26	1,5	1,6	0,49	<0.1	0,34	<0.1	0,13	0,50
D	LB	57	11	14	7,5	1,8	<0.1	3,4	3,0	0,74	<0.1	<0.1	<0.1	0,16	0,37
D	HL	85	4,8	4,0	3,7	0,33	<0.1	1,1	0,22	0,51	<0.1	<0.1	<0.1	<0.1	0,69
D	HL	82	9,2	3,3	2,8	0,17	0,15	1,2	0,67	<0.1	<0.1	<0.1	<0.1	0,20	0,29
D	HL	77	6,9	7,3	4,5	0,34	<0.1	1,7	1,3	0,39	<0.1	<0.1	<0.1	<0.1	0,41



Table 3. Mineralogy of specific soils according to Claquin et al. (1999) and Journet et al. (2014) and comparison with the one obtained in this study for six selected samples. Bulk, clay and silt fractions mineralogy (obtained from texture fractionation) and <10 µm and silt (10-63 µm) fractions mineralogy using fully dispersed separation. All content is in mass %.

	Carbonates					Clays					Salts		Fe-oxides	
	Qtz	Feld	Cal	Dol	Mca	Chl	Sme	Plg	Kln	Tot.clay	Gp	Hal	Hem	Gt
Bulk	58	9.5	15	2.4	6.4	1.0	0.1	0.2	3.8	11	0.2	8.1	0.5	0.5
Clay Ye Claquin	5	NA	6	NA	89	NA	NA	NA	NA	≈89	NA	NA	NA	NA
Clay Ye Journet	8	3	18	NA	67	NA	NA	1	3	≈71	NA	NA	NA	NA
Clay Fl Claquin	12	NA	11	NA	77	NA	NA	NA	NA	≈77	NA	NA	NA	NA
Clay Fl Journet	NA	NA	NA	NA	98	NA	NA	1	1	≈100	NA	NA	NA	NA
Clay classic Drâa	17	7.1	8.9	0.5	23	9.9	1.2	1.0	22	57	NA	NA	0.7	5.2
<10µm FD Drâa	23	4.7	19	2.4	19	4.7	0.4	0.2	14	38	NA	NA	2.2	1.8
Silt Ye Claquin	58	31	8	NA	NA	NA	NA	NA	NA	NA	2	NA	1	NA
Silt Ye Journet	43	21	20	NA	9	6	NA	NA	NA	15	NA	NA	1	NA
Silt Fl Claquin	30	38	29	NA	NA	NA	NA	NA	NA	NA	2	NA	NA	NA
Silt Fl Journet	39	19	12	NA	19	10	NA	NA	NA	29	NA	NA	1	NA
Silt classic Drâa	30	8	12	4.9	19	6.4	0.3	0.1	13	39	NA	NA	0.2	0.6
Silt FD Drâa	39	8.0	23	5.0	12	2.8	0.2	<0.1	7.5	23	NA	NA	1.2	0.7

Fl: Fluvisol sediment type; Ye: Yermosol; Qtz: Quartz; Feld: Feldspars; Cal: Calcite; Dol: Dolomite; Mca: Mica/illite; Chl: Chlorite; Sme: Smectite; Plg: Palygorskite; Kln: Kaolinite; Gp: Gypsum; Hal: Halite; Hem: Hematite; Gt: Goethite; FD: fully dispersed.